Modulation of Radar Observables by Upper Ocean Dynamics

Yan Yuan

TU Delft

Committee:
Dr.ir. Paco Lopez Dekker,
Dr.ir. Marcel Kleinherenbrink,
Ir. Christine Unal,
Ir. Marc Naeije

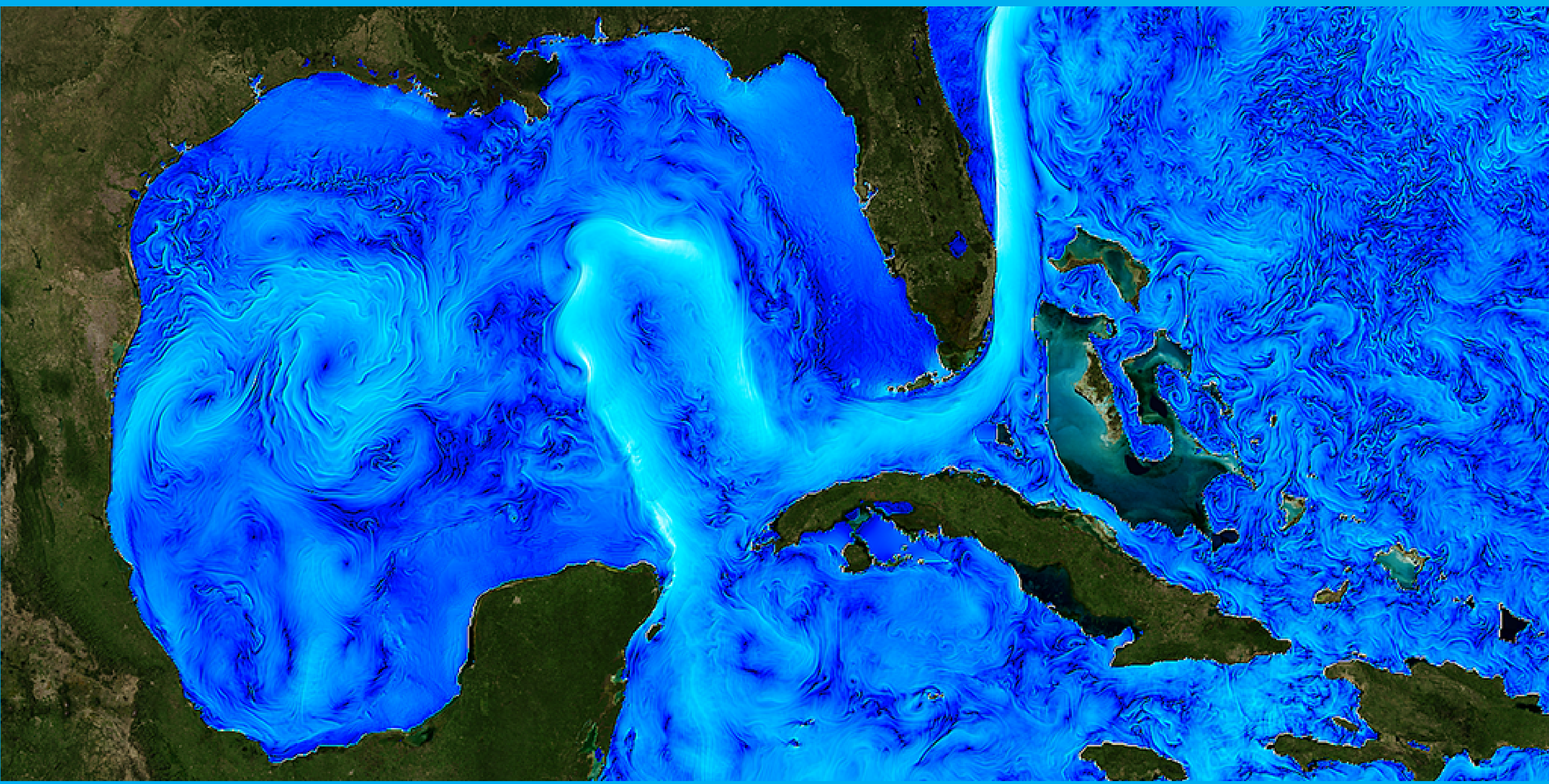

Modulation of Radar Observables by Upper Ocean Dynamics

by

Yan Yuan

to obtain the degree of Master of Science
at the Delft University of Technology,
to be defended publicly on Thursday November 26, 2020 at 11:45 AM.

Student number:	4812034	
Project duration:	December 1, 2019 – November 26, 2020	
Thesis committee:	Dr. ir. Paco Lopez Dekker,	TU Delft, chair
	Dr. ir. Marcel Kleinherenbrink,	TU Delft
	Ir. Christine Unal,	TU Delft
	Ir. Marc Naeije,	TU Delft

TU Delft

Preface

This thesis marks the end of my MSc study at TU Delft. I would like to give my sincere gratitude to my supervisors, friends, and family who offered me strong support and witnessed my improvements during these two years.

First of all, I would like to thank my greatest supervisors Paco Lopez Dekker and Marcel Kleinherenbrink. Thanks for giving me the precious opportunity to improve my research ability by working on this interesting topic. I appreciate every discussion we had and every expertise you gave. Thank Paco for guiding me to find the pleasure of doing research. Thank Marcel for supervising me for two years with patient and enthusiasm. I couldn't have finished this thesis without either of you.

Thanks to everyone in the Harmony team. Thank Gert Mulder, Lorenzo Lannini, and Yuanhao Li, for giving me generous advice within their field of expertise. Thanks to Andreas Theodosiou for helping me out when I was stuck by the workstation.

A lot of thanks to my friends in the Netherlands, thanks for offering me different ways of accompanying during the quarantine. Thanks for every "I believe you can do it" and every "I'm here". Thanks to my friends in China for always supporting me mentally even they are far apart.

Finally, thanks to my parents and brother, who always support me with love and understanding.

Yan Yuan
Delft, November 2020

Abstract

Oceans cover a significant part of the Earth's surface. The coupling between the upper ocean and the atmosphere is very complicated with defied theoretical understanding, while it is essential for climate studies, weather prediction, and marine ecosystems. With the advent of spaceborne Synthetic Aperture Radar (SAR) systems, surface signatures of ocean and atmospheric processes have been revealed. As winds blowing over the ocean excite the wind waves, all undulations of the ocean surface are assumed as waves in this study. The primary sources for ocean surface signatures in SAR images are waves that are created by the exertion of the local wind stress. Wind waves cause changes in the backscattered power due to three mechanisms: specular reflections, Bragg scattering, and a contribution from wave breaking. A statistical multi-static normalized radar cross-section (NRCS) background model in terms of the directional wave spectrum is developed, considering both Bragg and non-Bragg mechanisms for various polarization states. As the qualitative comparison between optical and SAR data reveals a significant correlation in sea surface signatures, a synthetic attempt is made to estimate the SAR signals from optical signatures. This is realized with the transformation of the wave spectrum in a nonuniform medium, as a consequence of surface currents, and varying near-surface wind fields. A comparison between modeled NRCS and observations is presented. This modulated NRCS model advances the quantitative interpretation of the upper ocean dynamics from satellite measurements.

Contents

1 Introduction

Oceanic phenomena, including internal waves, filaments, jets, meandering fronts, and eddies have various surface ocean signatures in terms of roughness and temperature that are amenable to measurements from spaceborne Synthetic Aperture Radar (SAR) and optical instruments Boccia et al. [2017]. To quantitative understand these upper ocean dynamics from SAR measurements, imaging models which describe the sea surface and the normalized radar cross-section (NRCS) have been previously developed by Alpers and Hennings [1984], Romeiser et al. [1997] and Kudryavtsev et al. [2005]. A synthetic attempt to analyze the radar signatures from infrared measurements proposed in Kudryavtsev et al. [2012] strengthens the quantitative retrieval of surface current characteristics. However, these models are restricted to mono-static observing geometry. To directionally quantify the radar signatures, a bistatic extension to the model is implemented for the Earth Explorer 10 candidate Harmony in this study.

1.1. Waves and currents

The wind is the main energy source for the upper ocean. It changes the sea surface roughness by exciting waves and generating surface currents and this results in the signatures in radar backscatter images. Waves serve as the base of modeling radar backscatter in a uniform sea surface with steady wind and no current present. Johannessen et al. [2005] argued that the currents have the potential to locally affect the short-scale surface wave energy, and thus resulting in enhanced or suppressed radar-detectable roughness changes. Therefore the currents are considered as a source of nonuniformity and modulate the NRCS.

Waves emerge as tiny undulations of the ocean surface and grow slowly in wavelength, speed, and amplitude with increasing wind speed and fetch Keller and Wright [1975]. Statistical descriptions of the waves are essential for understanding the interaction in the ocean-atmosphere interface. The most important formulation among them is the wave spectrum which stems from the early work of Phillips [1958] and is widely used for modeling the radar observations. The wave spectrum describes properties of a wave field as a function of wavelength and the propagation direction and it can be formulated as an energy balance between wind input, wave breaking dissipation, and wave-wave interaction redistribution processes. With the wave spectrum as the base, the mechanisms which contribute to the radar backscatter can be represented. It is generally accepted that the dominant mechanism of ocean waves contribution to radar backscatter for moderate incident angles (typically $20° - 60°$) is the electromagnetic waves resonance with ocean waves of comparable wavelengths, so-called Bragg scattering Wright [1968]. For small incident angles (<20°), the main mechanism is specular reflection Valenzuela [1978]. In addition to these, Lyzenga [1996] suggests that the wave breaking mechanism also has an important contribution, especially in storm conditions, to radar backscatter based on the experiment findings by Walker et al. [1996].

The currents are analyzed based on the Ekman motion theory. That is the friction force that acts on the sea surface via the wind, interacts with the quasi-geostrophic current (QGC) field, and thus generates secondary ageostrophic circulation (ASC), and thus produces convergence and divergence zones which are detectable by both microwave and optical sensors. The quasi-geostrophic currents refer to flows where the Coriolis force is almost balanced by pressure gradient force. The ASC generation is only by Ekman transport and diabatic mixing mechanisms in the Ekman layer according to Klein and Hua [1990] and Garrett and Loder [1981].

Ekman transport is a component of wind-driven ocean currents. Wind energy is transferred to the upper ocean by the friction effects and generates currents. With the Coriolis effect, the water does not move downwind but at a 90° angle from the direction of the wind. In the northern hemisphere, the transportation is deflected clockwise from the wind direction, while in the southern hemisphere is counterclockwise. For a cyclonic wind stress system in the northern hemisphere, which rotates anticlockwise, the mass transport at the upper ocean layer is deflected to the right of the rotation direction. Therefore, the Ekman transport is away from the center of the gyre and results in a divergent flow that gives rise to upwelling and bring the deeper cold waters to the surface. This is called Ekman suction as shown on the left of figure 1.1. On the contrary, the anti-cyclonic in the northern hemisphere will result in Ekman pumping, which results in a convergent flow that gives rise to downwelling of surface water as shown on the right side of the figure 1.1. Within the convergence zone, the sea surface is raised, while it is suppressed in the divergence zone. This slopes the sea surface around the convergence and divergence zones and generates signatures that are detectable for microwave radars.

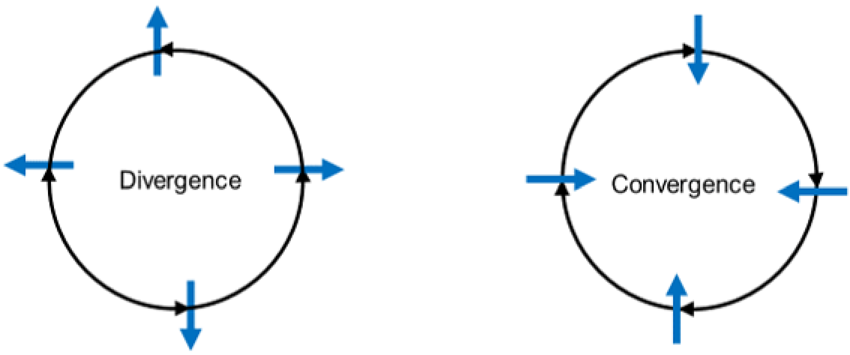

Figure 1.1: Ekman transport in the northern hemisphere: Ekman suction on the left, Ekman pumping on the right.

A balance between the pressure gradients, Coriolis, and turbulent drag forces at the upper ocean forms the surface Ekman layer, which reaches the depth of a few hundred meters (typically 50-200 m). The horizontal temperature gradient in the Ekman layer drives the diabatic mixing where the water exchanges the energy with its surroundings by virtue of a temperature difference between them. Together with the temperature gradients formed by Ekman transport, both are detected in the sea surface temperature measurements.

1.2. SAR observations

Spaceborne Synthetic Aperture Radar (SAR) is an active remote sensing system and it provides all-weather, day-and-night high-resolution images with both amplitude and phase information Moreira [2014]. The first spaceborne SAR experiments over oceans were carried out by Seasat in 1978. The wave features were found visible on the radar images. In the 1990s, the European Remote Sensing (ERS) satellites carrying SAR were launched which had a dedicated wave mode, tailored for wind and wave measurements Lehner et al. [2000]. Envisat was launched in 2002 with a more flexible wave mode Alpers [2003]. With extended polarization capability, the Radarsat-2 was launched in 2007. Today, the Sentinel-1 carrying C-band SAR is operating with larger swath ocean scenes Mouche and Chapron [2015]. In this study, the multi-static radar backscatter model over the ocean is constructed for the Earth Explorer 10 candidate Harmony, which will fly two identical C-band receive-only SAR satellites trailing and heading the illuminator Sentinel-1D López-Dekker et al. [2019].

The Sentinel-1 SAR images exhibit ocean surface signatures introduced in section 1.1. Figure 1.2 shows NRCS contrasts, which are computed as the ratio of short-wavelength and long-wavelength filtered NRCS variations. The contrasts images reveal typical ocean features, like currents, eddies and wind patterns. The first one exhibits a strong current, which will be used to validate the current modulation on NRCS in chapter 5. The positive/negative contrasts correspond to the convergence/divergence zone, while the white spots are noise caused by boats. The second one is an eddy contaminated by spilled oil, the core around −90.5° is visible. Both of these figures are found near the coast of the Western Gulf of Mexico. The third one which shows wind patterns together with temperature fronts is found in the Agulhas current area. The relatively smaller scale cells are organized large atmosphere eddies, while the larger scale horizontal strips are temperature fronts. In principle, the temperature-related signatures are visible in optical measurements too, but they are regularly covered by clouds in practice.

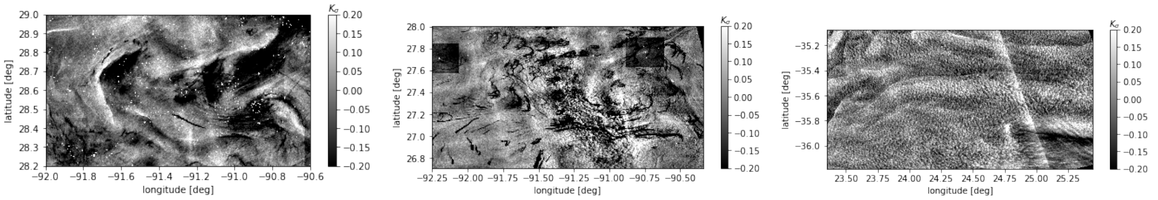

(a) (b) (c)

Figure 1.2: The image contrasts of sea surface signatures: (a) current, (b) eddy and (c) wind patterns with temperature fronts.

1.3. Research question

High-resolution SAR provides finely-detailed imagery of the mesoscale to submesoscale sea surface signatures. With a mono-static system, it loses the directional capability to quantify these signatures. One possible solution is using a multi-static observation configuration to derive quantitative information on these image patterns. Therefore, the research question in this study is specified as follows:

★ *How do surface features modulate the multi-static radar signatures of the ocean surface?*

To answer this, the following sub-questions are to be covered:

- How to represent the wave spectrum over the range of wave numbers that are relevant to radar observations?

  Through drag, wind acts on the ocean surface causing waves to grow and surface currents to change. These wind waves with different properties are responsible for different changes in the backscattered power. The wave spectrum, provides a statistical description of the wind waves, is closely related to the wind speed, wind direction and sea states. Therefore, the radar observations under varying conditions can be modeled from the wave spectrum.

- How to model backscatter for mono-static SAR and convert it to a bistatic system?

  Wind waves affect the backscattered power in three ways: specular reflection, Bragg scattering and wave breaking. With the wave spectrum as the input, the contribution of each mechanism to total radar backscatter is represented. Starting with the mono-static case, the co-polarized and cross-polarized backscatter models are constructed. The bistatic backscatter model is achieved by adjusting the mono-static geometry and by a rotation of the polarization.

- How do current features modulate the wave spectrum, and how do these translate to a modulation of the multi-static NRCS?

  The ocean current gradients alter the wave spectrum and thus modulate the NRCS in multi-static radar system. The sea surface temperature fronts represent the density gradients in the ocean and thus used to derive the ocean currents. Modulation from SST-derived currents used as a way to inspect the radar signatures.

1.4. Outline

The following chapters are organized with the sub-questions. Chapter 2 constructs the full wave number spectrum as the base for the multi-static backscatter model. Chapter 3 looks into details of each mechanism that contributes to the observed backscatter in a steady wind and no current condition. Chapter 4 applies the mono-static backscatter model to the bi-static geometry as a contribution to the Harmony project. Chapter 5 includes the currents effect to modulated the radar signatures of the ocean surface. The SST-derived currents is used to perform the modulation and qualitatively validated by radar observables. Chapter 6 summarizes the conclusions and gives recommendations for future work. A list of constants at the back helps with the re-implement of the equations in this study.

2

Wave spectrum

The directional wave spectrum is a statistic description of the wind-generated surface waves, which is often used in the study of air-sea interactions. In microwave remote sensing, often only short-scale roughness is considered, as it provides a proxy for the local wind stress, and it is important for modeling and understanding the signal observed by microwave sensors. However, current studies show that microwave measurements are also modeled by intermediate- and long-scale waves, and the interaction between different scales. In this chapter, two wave spectra derived from two different approaches are described. One is Elfouhaily wave spectrum which is derived from in-situ or tank measurements, another Kudryavtsev spectrum is based on the energy balance equation. As the long-wave part of the Kudryavtsev spectrum includes the wave-wave interaction which lacks theoretical understanding, only the short-wave spectrum is defined. The full wave number spectrum is a composition of the Kudryavtsev short-wave spectrum and Elfouhaily long-wave spectrum.

2.1. Elfouhaily wave spectrum

The Elfouhaily et al. [1997] unified spectrum is a relatively simple closed-form model for ocean surface directional wave spectrum, and it is solely based on in-situ or tank measurements and no radar data is included in elaborating this model. This spectrum is a combination of two regimes, the long-wave regime is formulated based on the Joint North Sea Wave Project (JONSWAP), while at the high wave numbers, the spectrum is based on the work of Phillips [1985] and Kitaigorodskii [1973]. Both regimes use similar, relatively simple, analytic descriptions, and stress the air-sea interaction process of friction between wind and waves is occurring at all wavelengths simultaneously. This full wave number model as a function of fetch can properly reproduce both fully developed and young sea conditions and to provide agreement with in-situ observations in the high wave number regime. Compared with in-situ and tank measurements, the Elfouhaily spectrum is validated from wave number near the main spectral peak k_p up to the gravity-capillary peak k_γ, this range is also the most interesting for radar applications.

2.1.1. Omnidirectional wave spectrum

The full omnidirectional wave spectrum is expressed as a sum of long- and short-wave regimes. Long-wave spectrum corresponds to the energy-containing range, in which turbulent kinetic energy per unit mass (TKE) is produced. Short-wave spectrum correspond to equilibrium range in the spectrum which is determined by the physical parameters that govern the continuity of the wave surface from Phillips [1958].

$$S(k) = k^{-3}[B_l + B_h], \tag{2.1}$$

where k is the wave number with unit rad per meter, $S(k)$ stands for sea surface elevation spectrum, B_l and B_h stand for curvature spectrum in low and high frequencies respectively. The demarcation point between these two regimes is $10k_p$, which was observed by Leykin et al. [1984] and the spectrum continuity is maintained by the wave side effect function inside of both terms. An illustration of the omnidirectional spectrum is given in figure 2.1 for wind speed from $5m/s$ to $15m/s$ with a $2m/s$ step.

Wave number at the main spectral peak is defined as

$$k_p = k_0\Omega_c^2, \tag{2.2}$$

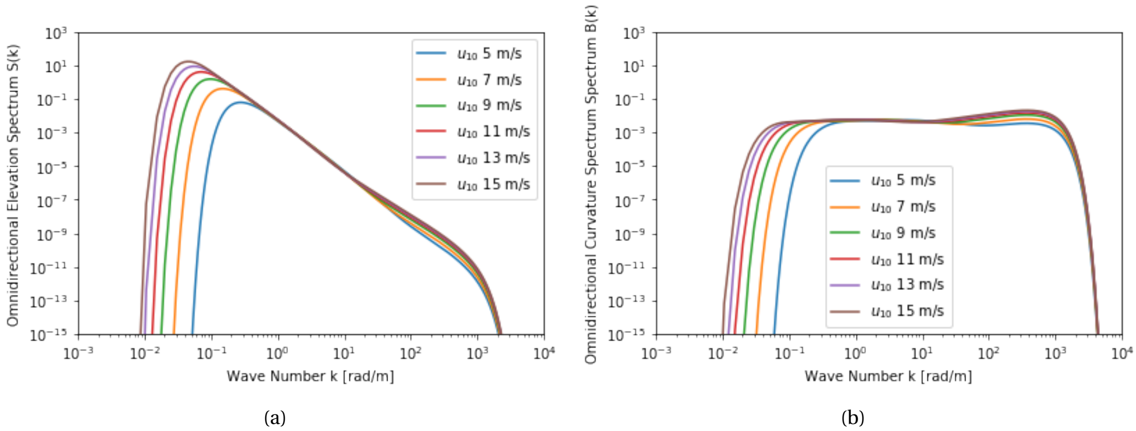

Figure 2.1: (a) Unified omnidirectional elevation spectrum $S(k)$ and (b) its corresponding curvature spectrum for the full wave number range and for wind speed from $5m/s$ to $15m/s$ under fully developed sea state.

where $k_0 = g/u_{10}$, $g = 9.80665m/s^2$ is the gravitational acceleration, u_{10} is the wind speed at a height of $10m$ above the water surface. From Hasselmann et al. [1973] and Donelan et al. [1985], Ω_c is the dimensionless inverse wave age which is empirically related to the dimensionless fetch X, with a theoretical inverse wave age 0.84 for fully developed sea,

$$\Omega_c = 0.84 \tanh[(X/X_0)^{0.4}]^{-0.75}, \tag{2.3}$$

where $X_0 = 2.2 \times 10^4$.

The long-wave curvature spectrum B_l corresponds to gravity waves having wave number up to $10k_p$, is expressed as

$$B_l(k, c_p/u_{10}) = \frac{1}{2}\alpha_p \frac{c_p}{c} F_p, \tag{2.4}$$

where $\alpha_p = 6 \times 10^{-3}\sqrt{\Omega}$ is the generalized Phillips-Kitaigorodskii equilibrium range parameter for long waves Phillips [1966], $c(k)$ is the long-wave phase speed and $c_p = c(k_p)$ is the phase speed at the spectral peak k_p. F_p is the long-wave side effect function, which is given by

$$F_p = L_{PM} J_p \exp\left\{-\frac{\Omega}{\sqrt{10}}\left[\sqrt{\frac{k}{k_p}} - 1\right]\right\}, \tag{2.5}$$

where first term $L_{PM} = exp\{-\frac{5}{4}(k_p/k)^2\}$ and second term $J_p = \gamma^{\Gamma}$ are standard Pierson Jr and Moskowitz [1964] and JONSWAP peak enhancement functions, respectively. The last exponential term behaves as a "cut-off" function to suppress B_l at wave numbers exceeding $10k_p$. According to Hasselmann et al. [1973] and Donelan et al. [1985], both α_p and F_p depend on the dimensionless inverse-wave-age parameter, which is defined as

$$\Omega = u_{10}/c_p. \tag{2.6}$$

The short waves actually determine the sea drag dictates the reliable statistical description of these waves, especially in the range of the short gravity and capillary range. Indeed, in the case of radar remote sensing, short gravity and capillary-gravity waves will serve as roughness elements on the sea surface which modulate the backscattered power of electromagnetic waves. The short-wave curvature spectrum B_h, is expressed as

$$B_h(k) = \frac{1}{2}\alpha_m \frac{c_m}{c} F_m, \tag{2.7}$$

where α_m is the generalized Phillips-Kitaigorodskii equilibrium range parameter for short waves Phillips [1966], which depends on the dimensionless parameter u_*/c_m, where u_* is friction velocity at water surface from Lees [2012], c is the short-wave phase speed and $c_m = 0.23m/s$ is the minimum phase velocity at the wave number associated with a supposed gravity-capillary peak in the curvature spectrum. To compute friction velocity, the drag coefficient c_g is defined equal to the square root of wind stress coefficients over the sea surface for all sea states proposed by Wu [1980]

$$c_g = \sqrt{(0.8 + 0.065u_{10}) \times 10^{-3}}. \tag{2.8}$$

Thus we can compute the friction velocity by

$$u_* = c_g u_{10}, \tag{2.9}$$

and α_m which is defined to fit the data of Jähne and Riemer [1990] and of Hara et al. [1994] as

$$\alpha_m = \begin{cases} 10^{-2}(1+\ln(u_*/c_m)) & u_* < c_m \\ 10^{-2}(1+3\ln(u_*/c_m)) & u_* > c_m \end{cases}. \tag{2.10}$$

The last term F_m is the long-wave side effect function, it counts for viscous cutoff and for the bandwidth of gravity-capillary waves. It is taken here as

$$F_m = L_{PM} \exp\left\{-\frac{1}{4}\left[\frac{k}{k_\gamma}-1\right]^2\right\}, \tag{2.11}$$

where k_γ is the wave number at gravity-capillary peak, is also known as the wave number of the minimum phase velocity, it can be written as

$$k_\gamma = \sqrt{g\rho_w/\gamma}, \tag{2.12}$$

where $\rho_w = 1000 kg/m^3$ is water density and $\gamma = 0.07275 J/m^2$ is the water surface tension.

2.1.2. Directional wave spectrum

The omnidirectional wave spectrum gives the energy density at each wave number, and obviously we need to add a spreading function to describe the directional wind-wave field, which is needed in both satellite remote sensing and atmosphere-ocean research. In order to inspect the directional distribution of the spectrum, a spreading function $\Phi(k,\varphi)$ from Elfouhaily et al. [1997] is implemented, hence the spectrum with angular spread can be defined as

$$\psi(k,\varphi) = \frac{1}{k} S(k)\Phi(k,\varphi), \tag{2.13}$$

where φ is the angle between the direction of the wave component and the wind, and the spreading function is given by

$$\Phi(k,\varphi) = \frac{1}{2\pi}[1+\Delta(k)\cos 2\varphi], \tag{2.14}$$

where $\Delta(k)$ is the downwind-crosswind ratio, for a unified full wave number approach, it can be written as

$$\Delta(k) = \tanh[a_0 + a_p(c/c_p)^{2.5} + a_m(c_m/c)^{2.5}], \tag{2.15}$$

where $a_0 = \frac{\ln 2}{4}$ and $a_p = 4$ are constants, and $a_m = 0.13\frac{u_*}{c_m}$. From these equations, it is clear that the spreading function $\Phi(k,\varphi)$ is symmetric about the downwind direction and has both wave number and wind speed dependence.

2.2. Kudryavtsev wave spectrum

Considering the disadvantage of no radar data is included in elaborating the Elfouhaily spectrum, we describe another spectrum from Kudryavtsev et al. [2003] to replace the short-wave spectrum in section 2.1. Kudyavtsev wave spectrum is a physical model of the short wind waves in the wavelength range from a few millimeters to a few meters. The evolution of the spectrum is defined by energy balance governing equations, considering energy input from the wind, viscosity dissipation, wave breaking processes, and wave-wave nonlinear interactions. As it will potentially describe the physical properties of the sea surface under the joint action of wind and surface currents, it is more appropriate to interpret high-resolution radar image contrasts from the SAR instrument.

2.2.1. Governing equations

The Kudryavtsev et al. [2003] wave spectrum is formulated from the energy balance equation which is define in terms of wave action spectrum $N(\mathbf{k})$ as

$$\frac{\partial N(\mathbf{k})}{\partial t} + (c_{gi} + u_i)\frac{\partial N(\mathbf{k})}{\partial x_i} - k_j \frac{\partial u_j}{\partial x_i}\frac{\partial N(\mathbf{k})}{\partial k_i} = Q(\mathbf{k})/\omega, \tag{2.16}$$

where c_{gi} and u_i are components of the wave group velocity and the surface current (i and $j = 1,2$), ω represents the intrinsic frequency is related to wave number vector $\mathbf{k}$ by the dispersion relation

$$\omega^2 = gk + \frac{\gamma}{\rho_w} k^3, \tag{2.17}$$

where $k = |\mathbf{k}|$ and $Q(\mathbf{k})$ is the energy source. The wave action spectrum $N(\mathbf{k})$ are related to curvature spectrum $B(\mathbf{k})$ which we will mainly work with via

$$N(\mathbf{k}) = \frac{\omega}{k^5} B(\mathbf{k}). \tag{2.18}$$

The sources and sinks in energy $Q(\mathbf{k})$ consist of the wind forcing energy input, viscous effects, wave-wave interactions' distribution from Holthuijsen [2010], dissipation via wave breaking and shorter wave generation by wave breaking. It is quite complicated, however, in the equilibrium range ($k > 10k_p$) of the spectrum, the energy source can be significantly simplified. Here we adopt the background model derived in Kudryavtsev et al. [2003], where quadruplet wave-wave interactions were ignored while three-wave interactions are assumed quadratic in wave spectrum. Together with the rate of energy dissipation proposed by Phillips [1985], the total energy source reads

$$Q(\mathbf{k}) = \omega^3 k^{-5} \left[\beta_v(\mathbf{k}) B(\mathbf{k}) - B(\mathbf{k}) \left(\frac{B(\mathbf{k})}{\alpha} \right)^n + I_{sw}(k) + I_{pc}(\mathbf{k}) \right], \tag{2.19}$$

where the first term represents the direct wind energy input determined by the friction velocity of the atmosphere which results from the interaction of wind and waves. The effective growth rate $\beta_v(\mathbf{k})$ is defined as the differences between the wind growth rate $\beta(\mathbf{k})$ and the rate of viscous dissipation, it can be written as

$$\beta_v(\mathbf{k}) = \beta(\mathbf{k}) - 4vk^2/\omega, \tag{2.20}$$

where $v = 1.15 \times 10^{-6} m^2/s$ is the kinematic viscosity coefficient of sea water. The growth rate parameter for short waves $\beta(\mathbf{k})$ is parameterized with angular dependence follows from the numerical study of Mastenbroek [1996], and its physical meaning is that within the frame of the sheltering mechanism of short wave generation, surface pressure acting on the forward slope is proportional to the square of the wind velocity component perpendicular to the wave crest. Here it is taken as

$$\beta(\mathbf{k}) = \beta(k,\varphi) = C_\beta (u_*/c)^2 \cos\varphi |\cos\varphi|, \tag{2.21}$$

where C_β is defined according to the parameterization of Stewart [1974],

$$C_\beta = 1.5(\rho_a/\rho_w)(\kappa^{-1}\ln(\pi/kz_0) - c/u_*), \tag{2.22}$$

where $\rho_a = 1.225kg/m^3$ is the air density, $\kappa = 0.4$ is the Von Karman constant, z_0 is the roughness scale parameterized as in Smith [1988]

$$z_0 = a_* u_*^2/g + a_v v_a/u_*, \tag{2.23}$$

where $v_a = 1.47 \times 10^{-5} m^2/s$ is the kinematic viscosity coefficient of air, $a_* = 0.018$ and $a_v = 0.1$ are coefficients.

The second term in equation (2.19) represents the nonlinear energy losses due to wave breaking and three wave-interactions at $k/k_\gamma \propto 1$. Parameter α and n are the main parameters of the model. Inside the gravity range ($10k_p < k < k_{wb} = 2\pi/0.3$ rad/m), the spectrum form results through a balance between wind input and small-scale breaking. Considering the spectral rate of dissipation of these waves in Kudryavtsev et al. [1999], n_g and α_g should be function of k/k_γ, here we take the values at the boundaries as $\alpha_g = 5 \times 10^{-3}$ and $n_g = 5$ respectively. In the capillary-gravity range ($k_\gamma/2 < k < k_\gamma$), a balance between wind input, viscous dissipation, and resonant three wave-wave interaction determined the spectrum form from Kudryavtsev et al. [1999]. The 3-wave interactions dominate the energy loss, and they are quadratic in the saturation energy density $B(\mathbf{k})$, so $n_\gamma = 1$. In the transitional interval ($k_{wb} < k < k_\gamma/2$), the energy losses are dominated by small-scale wave breaking which is accompanied by the emitting of parasitic capillaries. Since in this interval both gravity and surface tension govern wave dynamics, Kudryavtsev et al. [2003] suggest that both parameters are function of k/k_γ, and the $n(k/k_\gamma)$ function is

$$1/n = (1 - 1/n_g) f(k/k_\gamma) + 1/n_g, \tag{2.24}$$

where $f(k/k_\gamma)$ is a tuning function which has to satisfy $f \to 0$ at $k < k_{wb}$ and $f \to 1$ at $k \sim k_\gamma$ to realize the spectrum continuity. In order to fit wind exponent measurements from Banner et al. [1989] and Hwang [2011], f is defined as

$$f(k/k_\gamma) = [1 + \tanh(2(\ln k - \ln k_b))]/2, \tag{2.25}$$

where k_b is a wave number corresponding to the center of transitional interval which is fixed at $k_b = 1/4k_\gamma$. An illustration of $f(k/k_\gamma)$ function in the range $(10k_p < k < k_\gamma)$ is shown in figure 2.2(a). The k/k_γ dependence of α defined via $n(k/k_\gamma)$ is argued by Kudryavtsev et al. [2003]

$$\ln(\alpha(k/k_\gamma)) = \ln(a) - \ln(\bar{C_\beta})/n(k/k_\gamma), \tag{2.26}$$

where $\bar{C_\beta}$ is the growth rate parameter averaged over the transitional interval, and $a = 2.5 \times 10^{-3}$ is a tuning constant defined to fit the mean square slope to the results of Cox and Munk [1954] derived from optical glitter measurements. Both tuning parameters under $10m/s$ wind condition are shown in figure 2.2.

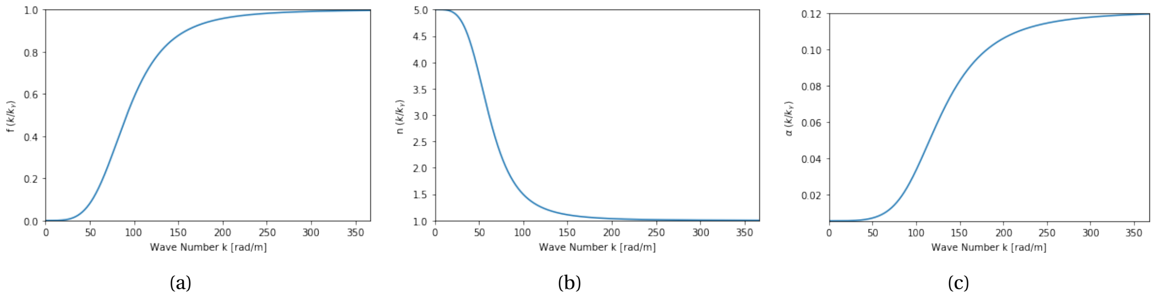

Figure 2.2: (a) Filter function $f(k/k\gamma)$. Tuning parameter functions (b) $n(k/k\gamma)$ and (c) $\alpha(k/k\gamma)$ when wind speed is $10m/s$.

The third term I_{sw} of equation (2.19) is the dimensionless rate of short wave generation by longer breaking waves$(k < k_{wb})$, they are disrupted with wave crests broken and generates both subsurface turbulence and enhanced isotropic surface roughness as described in Kudryavtsev and Johannessen [2004]. It is defined as

$$I_{sw} = \frac{c_b}{2\alpha_g}\omega \int\int_{k<k_{bm}} \omega\beta(\mathbf{k})B(\mathbf{k})d\ln k d\varphi, \tag{2.27}$$

where $c_b = 1.2 \times 10^{-2}$ is an empirical constant, $\alpha_g = 5 \times 10^{-3}$ is the tuning parameter inside the gravity range, $k_{bm} = min(k/10, k_{wb})$ is the upper limit of integration defining interval of breaking waves which generate shorter waves at wave number k. While the last term I_{pc} is the dimensionless short wave generation rate of short breaking waves$(k > k_{wb})$ which are not disrupted due to surface tension but produce trains of parasitic capillaries. According to Kudryavtsev et al. [2003], it is defined as

$$I_{pc}(\mathbf{k}) = \beta(\mathbf{k_g})B(\mathbf{k_g})\phi(k), \tag{2.28}$$

where $\mathbf{k_g}$ is the wave number of generating gravity waves, it is collinear with the wave numbers of parasitic capillaries $\mathbf{k}$, and their modulus are related as

$$k_g = k_\gamma^2/k. \tag{2.29}$$

As the parasitic capillaries are emitted in the transitional interval$(k_w b < k_g < k_\gamma/2)$, combined with equation (2.29) the cut-off of ϕ function is linked to the transitional wave number as

$$2k_\gamma < k < k_\gamma^2/k_{wb}. \tag{2.30}$$

Therefore, we follow Yurovskaya et al. [2013] on the assumption that $k_{pc}^h = k_\gamma^2/k_{wb}$, $k_{pc}^l = 2k_\gamma$, and the function ϕ is a band-pass filter defined as

$$\phi(k) = f(k/k_{pc}^l) - f(k/k_{pc}^h). \tag{2.31}$$

2.2.2. Directional short-wave spectrum

Inside the equilibrium range from the wave number $10k_p$ up to a wave number near k_γ includes short gravity-capillaries and gravity waves, they are generated by local wind and by wave breaking, so-called as wind waves. These waves play a dominant role in supporting the total momentum flux to the sea surface, also serve as roughness elements on the ocean surface to scatter electromagnetic waves. Another kind of wave is parasitic capillaries which are generated on the crests of the free propagating wind waves, and the balance among cascade generation, viscous dissipation, and non-linear dissipation determines the spectrum. To consider more physical mechanisms, Yurovskaya et al. [2013] assumes the equilibrium range wave spectrum is a superposition of wind-wave spectrum B_w and parasitic-capillary spectrum B_{pc},

$$B_s(\mathbf{k}) = B_w(\mathbf{k}) + B_{pc}(\mathbf{k}), \tag{2.32}$$

either $B_w(\mathbf{k})$ and $B_{pc}(\mathbf{k})$ are defined as solutions of energy balance equation (2.16) with considering different energy sources.

In the range of wind waves, the term I_{pc} is zero which can be inferred from the band-pass filter in equation (2.28). Therefore, at a uniform condition where no surface current presents and wind is steady, the wind-wave range spectrum can be found as a solution of the equation

$$Q[B(\mathbf{k})] = \omega^3 k^{-5}\left[\beta_v(\mathbf{k})B(\mathbf{k}) - B(\mathbf{k})\left(\frac{B(\mathbf{k})}{\alpha}^n\right) + I_{sw}(k)\right] = 0. \tag{2.33}$$

In the downwind directions, I_{sw} is small in comparison with wind energy input and can be ignored, then the solution of equation (2.33) is

$$B_w^d(\mathbf{k}) = B_w^d(k,\varphi) = \alpha[\beta_v(k,\varphi)]^{1/n}. \tag{2.34}$$

This is considered as reference spectrum. In the crosswind direction, $\beta_v(\mathbf{k}) \approx 0$ because of its angular dependence $\cos(\varphi)|\cos(\varphi)|$, then the first term in the bracket of equation (2.33) is zero. The crosswind wind-wave spectrum is

$$B_w^{cr}(k) \approx \alpha\left[\frac{I_{sw}(k)}{\alpha}\right]^{\frac{1}{n+1}}. \tag{2.35}$$

In the upwind directions where $\beta_v(\mathbf{k}) < 0$, one may anticipate the low spectra density, thus the second nonlinear term in equation (2.33) can be omitted, and B_w^{up} is formed with the balance of wave breaking and viscosity dissipation and interaction with opposing wind,

$$B_w^{up}(\mathbf{k}) \approx -\frac{I_{sw}(k)}{\beta_v(\mathbf{k})}. \tag{2.36}$$

In both B_w^{cr} and B_w^{up}, the term I_{sw} is computed with the reference spectrum B_w^d as the first guess. A combination of these three asymmetric solutions as $B_w = \max[B_w^d, \min(B_w^{cr}, B_w^{up})]$ provides the first guess for the total wave spectrum. Next iteration of the spectrum is defined by Yurovskaya et al. [2013] as

$$B_w^j = B_w^{j-1} - [Q(B_w)/(\partial Q/\partial B_w)]_{B_w = B_w^{j-1}}, \tag{2.37}$$

where $Q(B_w)$ is the total energy source function (2.33). The iterated wind-wave spectrum is shown in figure 2.3 (a) with solid lines from wind speed $5m/s$ to $15m/s$ with $5m/s$ step.

To compute the parasitic-capillary spectrum, the wind input energy is omitted, and the only energy input is the term I_{pc} which is balanced by viscous and non-linear dissipation. The solution from Yurovskaya et al. [2013] is

$$B_{pc}(\mathbf{k}) = \frac{\alpha}{2}\left[-4vk^2/\omega + \sqrt{(4vk^2/\omega)^2 + 4I_{pc}(\mathbf{k})/\alpha}\right], \tag{2.38}$$

with I_{pc} defined by equation (2.28) for the iterated result B_w. The superposition of the two spectra is shown in figure 2.3 (b) with dashed lines for different wind speed conditions. Compared two different sets of lines, the role of wave breaking in the superposition model is clearly emphasized in the high wave number range.

2.2.3. Full wavenumber spectrum

Considering the contribution of tilt and hydrodynamic effects, the spectrum of long energy-containing waves needs to be defined. Following the empirical spectrum proposed by Donelan et al. [1985] with the high-frequency cut-off correction F_c proposed by Elfouhaily et al. [1997], the energy at wave number exceeding $10k_p$ can be suppressed. Thus the full wave number spectrum is defined as a combination of equilibrium spectrum and energy-containing spectrum,

$$B(\mathbf{k}) = B_l(\mathbf{k}, c_p/u_{10}) + (1-F_c)B_s(\mathbf{k}), \tag{2.39}$$

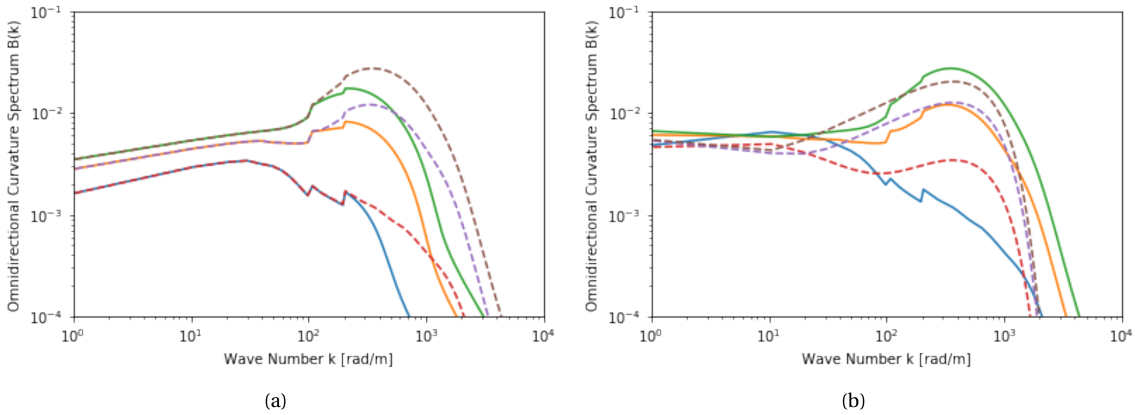

Figure 2.3: Spectrum for wind speed $u_{10} = 5m/s$, $u_{10} = 10m/s$ and $u_{10} = 15m/s$ form bottom to up.(a) Kudryavtsev short-wave spectrum, solid lines are wind-wave spectrum, while dashed lines are total short-wave spectrum.(b) Comparison of equilibrium range spectrum, solid lines are Kudryavtsev spectrum, while dashed lines are Elfouhaily spectrum.

where $F_c = \exp\left\{-\frac{\Omega}{\sqrt{10}}\left[\sqrt{\frac{k}{k_p}}-1\right]\right\}$ is the last term of function (2.5). The first term B_l is defined according to equation (2.4) and its spreading function in section 2.1.2, it can be written as

$$B_l(\mathbf{k}, c_p/u_{10}) = B_l(k, c_p/u_{10})\Phi(k,\varphi). \tag{2.40}$$

As Kudryavtsev's spectrum share the same long-wave regime with Elfouhaily's, only differences between the high wave range ($k > 10k_p$) spectrum are illustrated in figure 2.3 (b), solid lines are Kudryavtsev spectrum, while dashed lines are Elfouhaily spectrum. By taking into account radar measurements, the solid lines are less smooth than the empirical dashed curves. The differences in the range around $k < 1200$ rad/m between two sets of curves decreased with the increase of wind speed. Because the lack of side effect function which limits the behavior of Kudryavtsev's spectrum in the high wave number, the tails of the solid curves reach further than the dashed curves.

2.3. Conclusion

The curvature spectrum, $B(\mathbf{k})$, given in equation (2.39), will be used to establish the expressions of the backscatter model in the following chapters. It consists of two contributions. The first one, B_l, which is proposed by Elfouhaily et al. [1997] and given in equation (2.40), relates to the long-wave curvature spectrum. The second contribution, B_s, which is proposed by Kudryavtsev et al. [2003] and given in equation (2.32), relates to the short-wave curvature spectrum. For the long-wave spectrum, it is empirically derived from in-situ or tank measurements. For the short-wave curvature spectrum, it is constructed on the assumptions that the wind is steady and no currents present.

3

Mono-static ocean backscatter model

In this chapter, the full wave number spectrum proposed in equation (2.39) is used to model the mono-static radar backscattering from the sea surface. The observation geometry of the implemented mono-static radar system is illustrated in figure 3.1, where the satellite looks in the positive x-axis direction, θ_i is the incident angle, and φ is the azimuth angle defined with respect to the wind direction. As the spectrum behavior is

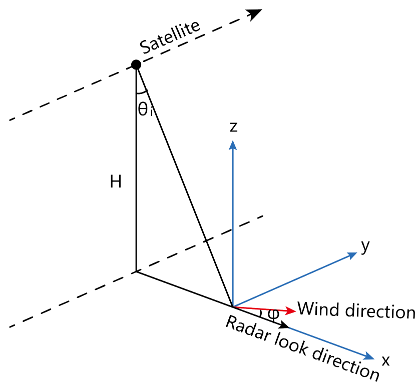

Figure 3.1: Mono-static geometry

related to the different mechanisms of energy sources, different wave number ranges are used to model main scattering mechanisms. This model includes Bragg scattering, specular reflection, and wave breaking in representing the NRCS of the sea surface and providing its statistical properties. At incident angle smaller than 20°, specular reflection from the sea surface dominates radar backscattering. With an increasing incident angle, its contribution becomes negligible in comparison with the Bragg scattering component. At moderate incident angles (typically 20° – 60°), Bragg scattering which is caused by resonant microwave scattering from rough surfaces plays the main role for radar backscattering. However, in high-resolution radar observations, the existence of "sea spikes" reveals that Bragg theory is not fully appropriate to represent and explain the radar signals at moderate incident angles, examples are given by Quilfen et al. [1999] and Horstmann et al. [2000]. In this study, wave breaking events generated intensive roughness is described to explain this. In the last section, the total NRCS and comparison with observations are illustrated to inspect the model performances.

3.1. Bragg scattering

Resonant between the radar waves and features at the water surface is called Bragg scattering. Regular periodic ocean waves with certain wavelengths allow a coherent superposition of reflections from the sea surface and thus form the interference where the constructive interference can strongly reinforce the echo signals in the direction of the radar receiver as illustrated in figure 3.2 by Wolff [2012].

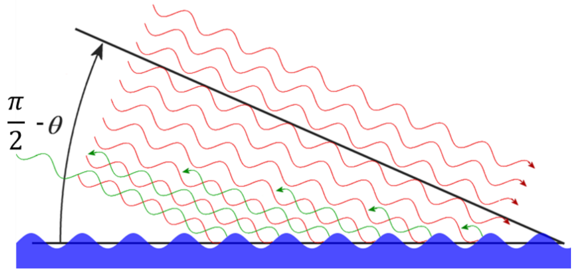

Figure 3.2: Under certain conditions, constructive interference reinforces weak individual reflections.

At moderate incident angles (typically 20 – 60°), radar backscattering theory proposed by Plant [1990] is based on the mechanism of resonant (Bragg) microwave scattering from a random rough surface. Here a composite Bragg scattering model from Kudryavtsev et al. [2003] is applied, which includes the resonant scattering due to the surface waves with the wavelength of the order of the electromagnetic wavelength, superposed on longer underlying tilting waves. This model is written as

$$\sigma^p_{\mathrm{Br}}(\theta,\varphi) = \int_\Gamma \sigma^p_{0\mathrm{Br}}(\theta - \arctan\eta_i, \varphi) P(\eta_i) d\eta_i, \tag{3.1}$$

where θ is the incident angle, η_i is the sea surface slope in the direction of the incident plane, $\sigma^p_{0\mathrm{Br}}$ is the pure Bragg scattering without superposed on long tilting waves as a function of incident angle and azimuth angle, the superscript p represents different polarization states. In real conditions, the pure Bragg theory loses its validity, as short wind waves scattering radio waves are running along with longer surface waves, and this phenomenon is indicated from models developed by Bass et al. [1968] and Wright [1968]. Therefore, a one-dimensional probability density function of sea surface slope along the incident plane $P(\eta_i)$ is introduced, and we follow Kudryavtsev et al. [2005] in assuming that it is Gaussian distributed with zero mean and a standard deviation, s_{η_i}, derived from wave spectrum. The tilting effect from across the incident plane is not considered, because it does not contribute significantly to the NRCS at small and moderate incident angles from Plant [1990].

For a pure Bragg process, the normalised radar cross-section σ^p_{0br} reads

$$\sigma^p_{0\mathrm{Br}}(\theta', \varphi) = 16\pi k_r^4 |G_p(\theta')|^2 S_r(k_{\mathrm{Br}}, \varphi), \tag{3.2}$$

where k_r is the radar wave number, G_p is the Bragg scattering geometric coefficient as a function of local incident angle $\theta' = \theta - \arctan\eta_i$, which is illustrated in figure 3.3. The last term $S_r(k_{\mathrm{Br}}, \varphi)$ is the folded spectrum

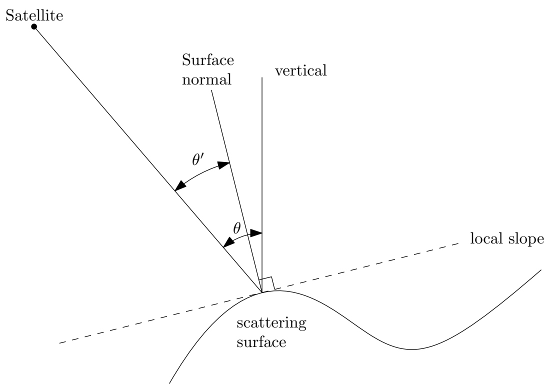

Figure 3.3: Reference geometry for the incident angle θ and for the local incident angle θ'.

of sea surface elevation with the local wave number of the Bragg waves $k_{\mathrm{Br}} = 2k_r \sin\theta'$ and azimuth angle φ. It is related to the directional wave number spectrum $S(k_{\mathrm{Br}}, \varphi)$ by

$$S_r(k_{\mathrm{Br}}, \varphi) = 0.5(S(k_{\mathrm{Br}}, \varphi) + S(k_{\mathrm{Br}}, \varphi + \pi)), \tag{3.3}$$

and $S(k_{\text{Br}},\varphi)$ is related to the curvature spectrum in equation (2.39) as

$$S(k_{\text{Br}},\varphi)=\frac{1}{k_{\text{Br}}^4}B(k_{\text{Br}},\varphi). \tag{3.4}$$

The geometric scattering coefficient is given by Plant [1990], for the vertical dual-polarization

$$G_{vv}(\theta')=\frac{(\varepsilon_r-1)[\varepsilon_r(1+\sin^2\theta')-\sin^2\theta']\cos^2\theta'}{[\varepsilon_r\cos\theta'+\sqrt{\varepsilon_r-\sin^2\theta'}]^2} \tag{3.5}$$

and for the horizontal dual-polarization

$$G_{hh}(\theta')=\frac{(\varepsilon_r-1)\cos^2\theta'}{[\cos\theta'+\sqrt{\varepsilon_r-\sin^2\theta'}]^2}. \tag{3.6}$$

Here $\varepsilon_r=73+18i$, the relative dielectric constant of $25°C$ pure water at a frequency of 5.35 GHz from Barthel et al. [1991], results in complex geometric scattering coefficients. The squared absolute values of both coefficients $|G_p(\theta')|^2$ are illustrated in figure 3.4 with the slope along incident plane in the range $[-3\sigma,3\sigma]$, σ is the standard deviation of $P(\eta_i)$.

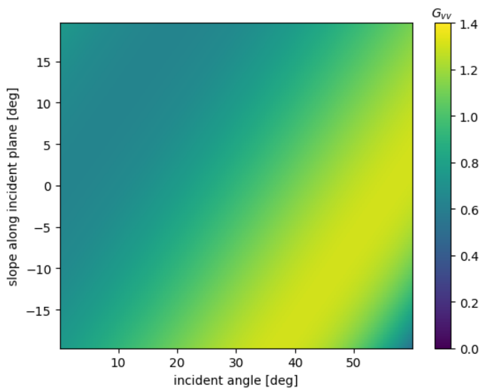

(a)

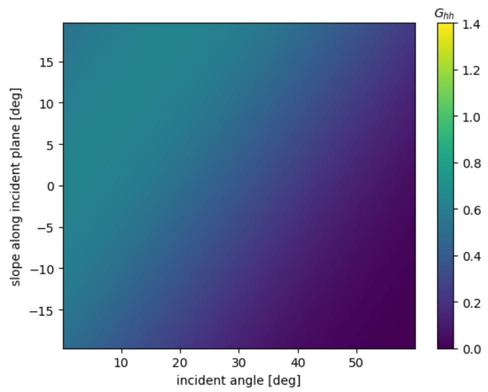

(b)

Figure 3.4: Squared absolute geometric scattering coefficients for (a) vertical polarization $|G_{vv}(\theta')|^2$ and (b) horizontal polarization $|G_{hh}(\theta')|^2$ with the slope along incident plane in the range $[-3\sigma,3\sigma]$.

In the composite model, wave number $k_d=d\cdot k_r$ is used to divide the wave spectrum into two intervals. Small-scale waves with $k_{\text{Br}}\geq k_d$ provide resonant (Bragg) scattering, thus the standard deviation of sea surface slope is

$$s_{\eta_i}=\sqrt{\int_{k_d}^{k_\gamma}\int_{-\pi}^{\pi}k^2\cos^2\varphi\Psi(k,\varphi)k\,dk\,d\varphi}, \tag{3.7}$$

where $\Psi(k,\varphi)=\frac{S(k,\varphi)}{k}$, and $P(\eta_i)$ can be written as

$$P(\eta_i)=\frac{e^{-\frac{\eta_i^2}{2s_{\eta_i}^2}}}{s_{\eta_i}\sqrt{2\pi}}. \tag{3.8}$$

Moreover, the integration limit Γ is deduced from the condition

$$2k_r\sin|\theta-\arctan\eta_i|\geq k_d, \tag{3.9}$$

in the domain of integration over the sea surface slope

$$\Gamma=\left[\eta_i\leq\tan(\theta-d/2)\cup\eta_i\geq\tan(\theta+d/2)\right], \tag{3.10}$$

where $d = 1/4$ is given in Thompson [1988]. While large-scale waves $k_{br} < k_d$ affect the scattering via random changes in the local incident angle and rotation of the incident plane, therefore if the condition in (3.10) is not fulfilled, the radar return is contributed by means of specular reflection. The composite Bragg models for both dual-polarization states in C-band with $10m/s$ wind speed, fully-developed sea condition are illustrated in figure 3.5. With the same magnitude scale from $-30dB$ to $2dB$, the horizontal polarized Bragg scattering is smaller than vertical polarized, the dip at around 5° indicates the effect of the integration limit in (3.8).

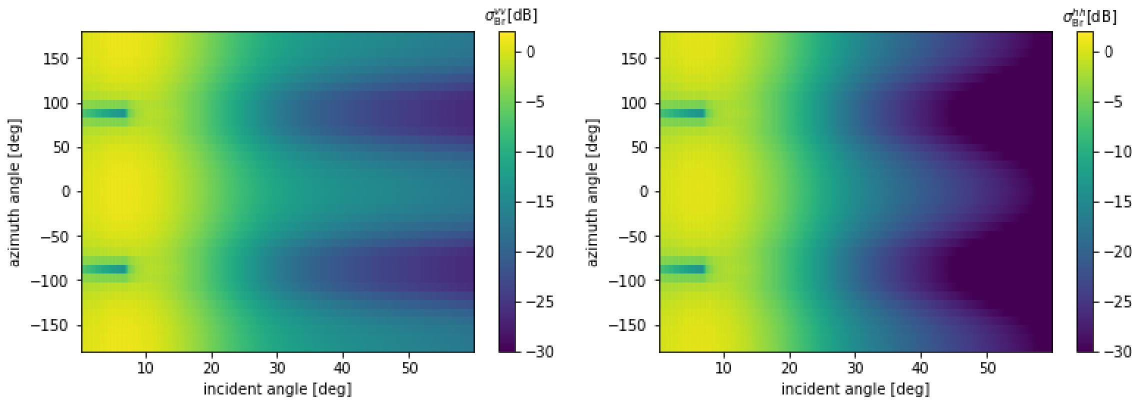

(a) (b)

Figure 3.5: C-band composite Bragg scattering model in fully-developed sea with wind speed $u_{10} = 10m/s$ condition for (a) vertical polarization $\sigma_{br}^{vv}(\theta,\varphi)$ and (b) horizontal polarization $\sigma_{br}^{hh}(\theta,\varphi)$.

For cross-polarization state, an empirical approximate model from Valenzuela [1978] is implemented,

$$\sigma_{\text{Br}}^{pq}(\theta,\varphi) = \pi \tan^{-4}\theta |G_{pp} - G_{qq}|^2 \frac{s_n^2}{\sin^2\theta} \times B(k_{\text{Br}},\varphi), \tag{3.11}$$

where s_n^2 is the mean square slope (MSS) of tilting waves out of the direction of incident plane, and it is defined from Kudryavtsev et al. [2019] as

$$s_n^2 = 2.25 \times 10^{-3} \ln(\Omega_\alpha^{-2} k_d u_{10}^2/g), \tag{3.12}$$

where $\Omega_\alpha = u_{10}\sqrt{k_p/g}$ is the inverse wave age of wind seas. This cross-polarization model is validated from 20° to 60° incident angles. The modeled Bragg scattering in C-band with $10m/s$ wind speed, fully-developed sea condition is shown in figure 3.6. From the magnitude scale, it is clear that the cross-polarized Bragg scattering signals are much smaller than that in dual-polarized states. Although σ_{Br}^{pq} shows the same symmetric property with the downwind direction, in the upwind direction, the NRCS is smaller than in the crosswind direction.

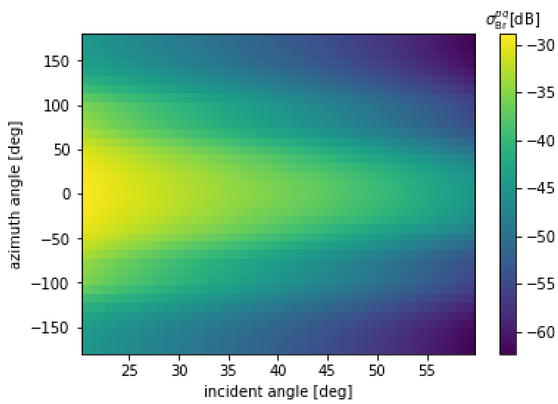

Figure 3.6: C-band Bragg scattering model in fully-developed sea with wind speed $u_{10} = 10m/s$ condition for cross-polarization $\sigma_{br}^{pq}(\theta,\varphi)$.

3.2. Specular reflection

Specular reflection is a mirror-like reflection of waves as shown in figure 3.7. Each reflected at the same angle to the surface normal as the incident ray, but on the opposing side of the surface normal in the incident plane formed by incident and reflected rays.

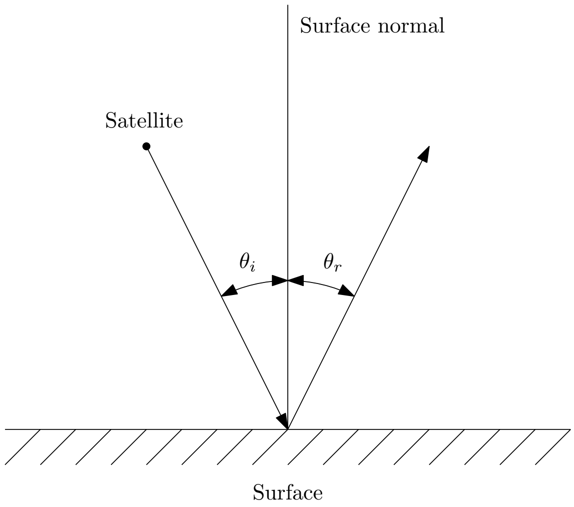

Figure 3.7: Specular reflection, θ_i is angle of incidence while θ_r is angle of reflection, $\theta_i = \theta_r$

Specular reflection together with Bragg scattering describes the radar scattering from a non-breaking wavy sea surface. At incident angles smaller than 20°, specular reflection is the main mechanism responsible for radar backscattering. As suggested by Kudryavtsev et al. [2005], its contribution can be modeled by

$$\sigma_{\mathrm{sp}}(\theta,\varphi) = \pi R_p^2(\theta') \sec^4\theta \cdot P(\eta_i,\eta_n)|_{\eta_i=\tan\theta,\eta_n=0}, \tag{3.13}$$

where $R_p^2(\theta')$ is the reflectivity (power reflection coefficient) defined in terms of the Fresnel reflection coefficients by equation (5.56) in Woodhouse [2005],

$$R_p^2(\theta') = |R_{xx}(\theta')|^2, \tag{3.14}$$

where $R_{xx}(\theta')$ is Fresnel reflection coefficients, and xx stands for different polarization states, it is defined as

$$R_{HH}(\theta') = \frac{\cos\theta' - \sqrt{\varepsilon_r - \sin^2\theta'}}{\cos\theta' + \sqrt{\varepsilon_r - \sin^2\theta'}} \tag{3.15}$$

for horizontal polarization, and

$$R_{VV}(\theta') = \frac{\varepsilon_r\cos\theta' - \sqrt{\varepsilon_r - \sin^2\theta'}}{\varepsilon_r\cos\theta' + \sqrt{\varepsilon_r - \sin^2\theta'}} \tag{3.16}$$

for vertical polarization from Plant [1990]. Here, $\theta' = \theta - \arctan\eta_i$ is the local incident angle. In the case of specular reflection, $\eta_i = \tan\theta$, thus θ' is zero, which means normal incidence. Under this condition, polarization states no longer make differences in the absolute magnitude of the reflection coefficients.

The function $P(\eta_i,\eta_n)$ is two dimensional probability density function of the sea surface slope along (η_i) and across (η_n) the incident plane. It is generally accepted that the probability density function of the sea surface slope in specular reflection mechanism is near Gaussian, thus

$$P(\eta_i,\eta_n) = \frac{1}{2\pi\sqrt{\Delta_2}} e^{\left(-\frac{\bar{\eta}_n^2\eta_i^2 - 2\overline{\eta_i\eta_n}\eta_i\eta_n + \bar{\eta}_i^2\eta_n^2}{2\Delta_2}\right)}. \tag{3.17}$$

To compute this, one needs to know the up- and cross-wind component of the mean square slopes. Based on Elfouhaily et al. [1997], and combined with the condition of large-scale waves mentioned in section 3.1, when the wave number is smaller than k_d, specular reflection plays the main role in radar scattering, we can write

$$s_{\mathrm{up}}^2 = \int_0^{k_d} \int_{-\pi}^{\pi} k_{\mathrm{Br}}^2 \cos^2 \varphi \Psi(k_{\mathrm{Br}}, \varphi) k_{\mathrm{Br}} d k_{\mathrm{Br}} d\varphi \tag{3.18}$$

$$s_{\mathrm{cr}}^2 = \int_0^{k_d} \int_{-\pi}^{\pi} k_{\mathrm{Br}}^2 \sin^2 \varphi \Psi(k_{\mathrm{Br}}, \varphi) k_{\mathrm{Br}} d k_{\mathrm{Br}} d\varphi, \tag{3.19}$$

where s_{up}^2 and s_{cr}^2 are MSS in the upwind and crosswind direction respectively. Based on both, elements of $P(\eta_i, \eta_n)$ can be expressed as

$$\overline{\eta_i^2} = s_{\mathrm{up}}^2 \cos^2 \varphi + s_{\mathrm{cr}}^2 \sin^2 \varphi \tag{3.20}$$

$$\overline{\eta_n^2} = s_{\mathrm{cr}}^2 \cos^2 \varphi + s_{\mathrm{up}}^2 \sin^2 \varphi \tag{3.21}$$

$$\overline{\eta_i \eta_n} = (s_{\mathrm{up}}^2 - s_{\mathrm{cr}}^2) \cos\varphi \sin\varphi \tag{3.22}$$

$$\Delta_2 = \overline{\eta_n^2 \eta_i^2} - (\overline{\eta_i \eta_n})^2 = s_{\mathrm{up}}^2 s_{\mathrm{cr}}^2, \tag{3.23}$$

where φ is radar look direction with respect to the wind. Considering the conditions of specular reflection ($\eta_i = \tan\theta, \eta_n = 0$), the probability density function is reduced to

$$P(\eta_i, \eta_n)|_{\eta_i = \tan\theta, \eta_n = 0} = \frac{1}{2\pi s_{\mathrm{up}} s_{\mathrm{cr}}} e^{\left(-\frac{\tan^2\theta}{2 s_{\mathrm{sp}}^2}\right)}, \tag{3.24}$$

where $s_{\mathrm{sp}}^2 = s_{\mathrm{up}}^2 s_{\mathrm{cr}}^2 / (s_{\mathrm{cr}}^2 \cos^2\varphi + s_{\mathrm{up}}^2 \sin^2\varphi)$ is the mean square slope satisfying conditions of the specular reflection. Above all, radar scattering contributed by specular reflection can be written as

$$\sigma_{\mathrm{sp}}(\theta, \varphi) = \frac{R_p^2 \sec^4\theta}{2 s_{\mathrm{up}} s_{\mathrm{cr}}} e^{\left(-\frac{\tan^2\theta}{2 s_{\mathrm{sp}}^2}\right)}. \tag{3.25}$$

The C-band specular reflection model under $10m/s$ wind speed, fully-developed sea condition is illustrated in figure 3.8. It is clear when the incident angle increases, the NRCS decreases dramatically, especially above 30°, the specular reflection contribution is negligible.

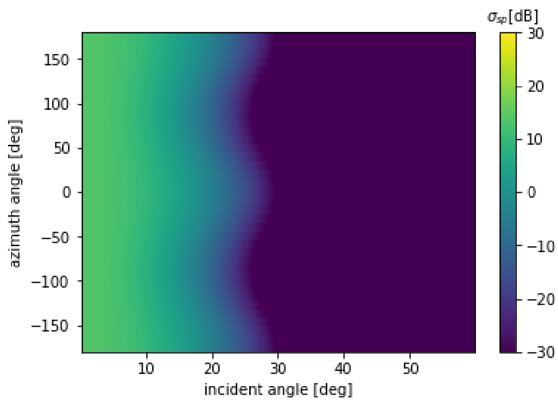

Figure 3.8: C-band specular reflection model in fully-developed sea with wind speed $u_{10} = 10m/s$ condition.

3.3. Wave breaking

Another non-Bragg scattering mechanism besides specular reflection is wave breaking, which is a very complicated phenomenon with defied theoretical understanding. To model its contribution to the radar return power, we follow the concept of Wetzel [1986] and Wetzel [1990]] who propose that breaking is mainly supported by spilling breakers as described by the plume model. We follow Kudryavtsev et al. [2003] in assuming that the radar returns from breaking waves are a sum of a discrete set of rough wave breaking patterns' contribution to increased radar backscatter. Additionally, the overall contribution of breaking waves is related to the wave breaking front statistics proposed by Phillips [1985]. Moreover, according to the observations of Ericson et al. [1999], we suggested that wave breaking does not depend on polarization. Thus, the NRCS contributed by an individual wave breaking zone is the same for dual-polarization,

$$\sigma_{\mathrm{wb}}(\theta,\varphi) = \sigma_{0\mathrm{wb}}(\theta)\cdot(1+M_{\mathrm{twb}}\overline{\theta_{\mathrm{wb}}}A_{\mathrm{wb}}(\varphi)), \tag{3.26}$$

where $\sigma_{0\mathrm{wb}}(\theta)$ is the NRCS of the plumes as a function of incident angle. The second term in the bracket represents the tilting effect of enhanced surface roughness due to the spread plumes on the forward face of breaking waves. The tilting transfer function $M_{\mathrm{twb}} = (1/\sigma_{0\mathrm{wb}})\partial\sigma_{0\mathrm{wb}}/\partial\theta$ is negative, therefore the contribution of wave breaking to the total NRCS is minimal in the downwind direction and maximal in the upwind direction. The constant $\overline{\theta_{\mathrm{wb}}}$ is the mean tilt of the non-Bragg scattering area, as we follow Kudryavtsev et al. [2003] in assuming that all scattering area is approximately the same, it is fixed as $\overline{\theta_{\mathrm{wb}}} = 5\cdot10^{-2}$ to match upwind to downwind radar observations by Unal et al. [1991], Jones and Schroeder [1978] and Masuko et al. [1986]]. The last term $A_{\mathrm{wb}}(\varphi)$ is the angular distribution of scattering from breaking waves and it provides deference between upwind and downwind NRCS.

Wave breaking involves highly nonlinear hydrodynamics on a wide range of scales, from gravity surface waves to capillary waves, down to turbulence from Holthuijsen [2010]. The model we use is based on Kudryavtsev et al. [2003], where they assume that only breakers with scales exceeding the radar wavelength can contribute to the radar returns, it means the breaker wave number upper limit is $k_{nb} = b_r k_r$, with $b_r = 0.1$. Additionally, in the case of short radio waves (e.g. K-band), k_{nb} relates to too short gravity waves, which rather generate Bragg theory-based parasitic capillaries than generate turbulent breakers. Therefore, the upper limit is further defined as $k_{nb} = \min(b_r k_r, k_{\mathrm{wb}})$. Moreover, the wave spectrum and statistic properties of breaking waves follow developments by Kudryavtsev et al. [1999], which only give results to short waves, thus we follow the assumption in Elfouhaily et al. [1997] that the lower limit of integral in wave breaking model is $10k_p$.

Inside the wave breaking range, the NRCS of the plumes is combined by the contribution of plume sides, which is proportional to $\varepsilon_{\mathrm{wb}} s_{\mathrm{wb}}^{-2}$, and its cap. Since these two parts are independent, $\sigma_{0\mathrm{wb}}(\theta)$ is estimated by Kudryavtsev et al. [2003] as

$$\sigma_{0\mathrm{wb}}(\theta) = \left(\frac{\sec^4\theta}{s_{\mathrm{wb}}^2}\right)e^{\left(-\frac{\tan^2\theta}{s_{\mathrm{wb}}^2}\right)} + \frac{\varepsilon_{\mathrm{wb}}}{s_{\mathrm{wb}}^2}, \tag{3.27}$$

here s_{wb}^2 is the mean square slope of enhanced roughness (assumed isotropic) of the wave breaking zone, $\varepsilon_{\mathrm{wb}}$ is the ratio of vertical to horizontal scale of the breaking zone. They are universal constants chosen to be $s_{\mathrm{wb}}^2 = 0.19$ and $\varepsilon_{\mathrm{wb}} = 5\times10^{-3}$ respectively to fit the experiment data reported by Unal et al. [1991] and Masuko et al. [1986], and known estimates of the sea surface NRCS at grazing angles.

To compute the angular distribution $A_{\mathrm{wb}}(\varphi)$, the wave breaking statistics proposed by Phillips [1985] is applied, which introduce the total length of breaking fronts $\Lambda(c)dc$ running with the velocities in the range from c to $c+dc$. Transforming the distribution $\Lambda(c)$ from c-space to k-space for short-wave range is

$$\Lambda(k,\varphi) = \frac{1}{2k}\left(\frac{B(k,\varphi)}{\alpha(k)}\right)^{n(k)+1}, \tag{3.28}$$

where $\alpha(k)$ and $n(k)$ are tuning parameters computed from equation (2.26) and (2.24) respectively. With equation (3.24), the distribution in azimuth of non-Bragg scatter $A_{\mathrm{wb}}(\varphi)$ can be written as

$$A_{\mathrm{wb}}(\varphi) = \Lambda_k^{-1}\int\cos(\varphi_1-\varphi)\Lambda d\varphi_1, \tag{3.29}$$

where φ_1 is the azimuth of breaking area respective to the azimuth φ, and its corresponding distribution is $\Lambda(k,\varphi_1) = \frac{1}{2k}(\frac{B(k,\varphi_1)}{\alpha})^{n+1}$. The term outside the integral, $\Lambda_k = \int\Lambda(k,\varphi_1)d\varphi_1$, is the distribution of breaking front lengths integrated over all directions. Both Λ and Λ_k have the same k dependence and they cancel out as numerator and denominator respectively, thus A_{wb} doesn't have wave number dependence.

The C-band wave breaking model under $10m/s$ wind speed, fully-developed sea condition is illustrated in figure 3.9. The azimuth angle dependence is completely different as Bragg scattering and specular reflection, because of the tilting transfer function M_{twb}.

An empirical expression for cross-polarized NRCS of an individual breaking zone in C-band, $\sigma_{\mathrm{wb}}^{pq}$, is derived in Kudryavtsev et al. [2019] as

$$\sigma_{\mathrm{wb}}^{pq}(\theta) = \pi\frac{|G_{pp}(\theta)-G_{qq}(\theta)|^2}{\tan^4\theta}\frac{s_{\mathrm{wb}}^2}{2\sin^2\theta}B_{\mathrm{wb}}, \tag{3.30}$$

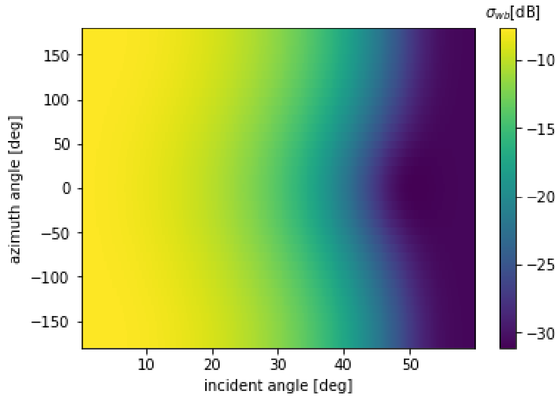

Figure 3.9: C-band co-polarization wave breaking model in fully-developed sea with wind speed $u_{10} = 10m/s$ condition.

where $G_{pp}(\theta)$ and $G_{qq}(\theta)$ are the geometric scattering coefficients in equation (3.5) and (3.6), but as functions of incident angles. The saturation spectrum is set to a constant $B_{\text{wb}} = 10^{-2}$. The validity of this model is from 20° to 60° incident angles, assuming uniformly directional distribution, the modeled wave breaking contribution in C-band is shown in figure 3.10. From the magnitude scale, the cross-polarized wave breaking NRCS is significantly smaller than that in dual-polarized states.

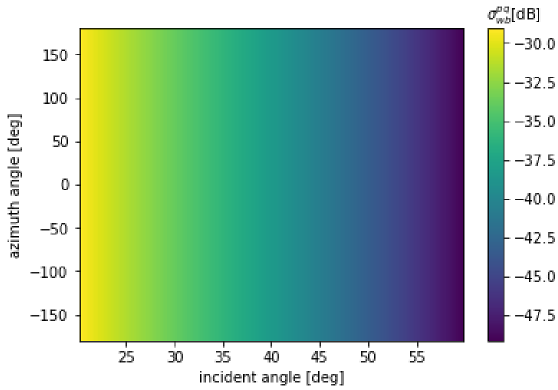

Figure 3.10: C-band empirical cross-polarization wave breaking model.

3.4. Total NRCS

The total observed NRCS from the sea surface is a sum of radar scattering from a regular non-breaking surface and a number of wave breaking zones. Kudryavtsev et al. [2003] suggested this description is also valid outside the breaking zone, and radar returns from breaking waves are proportional to the roughness enhanced surface, which is caused by wave breaking, at moderate incident angles. Hence, the NRCS due to Bragg scattering and specular reflection is restricted by a factor $1-q$, where q is the fraction of the sea surface covered by the wave breaking zone. The remaining sea surface with a fraction q provides wave breaking scattering and statistical properties of these enhanced roughness areas. Thus the total observed NRCS from a surface with ocean waves is modeled as

$$\sigma_0^p = \sigma_{0R}^p(1-q) + \sigma_{\text{wb}}q, \tag{3.31}$$

where $\sigma_{0R}^p = \sigma_{\text{Br}}^p + \sigma_{\text{sp}}$ represents the regular surface scattering contributed by Bragg scattering and specular reflection. The second term describes the total contribution from all the breaking fronts to the sea surface NRCS. The main tuning parameter of wave breaking scattering part q is described as

$$q = c_q \int_\varphi \int_{k<k_{nb}} \Lambda(k,\varphi_1)\,d\varphi_1\,dk, \tag{3.32}$$

where $c_q = 10.5$.

The total NRCS for dual polarization in C-band in a fully-developed sea with $10m/s$ wind speed is illustrated in figure 3.11. After the combination of three mechanisms, the horizontal polarization still keeps its smaller magnitude and fast decreasing with increasing incident angle features, while the dips in figure 3.5 at small incident angles are smoothed. To explain this and to inspect the contributions of different mechanisms

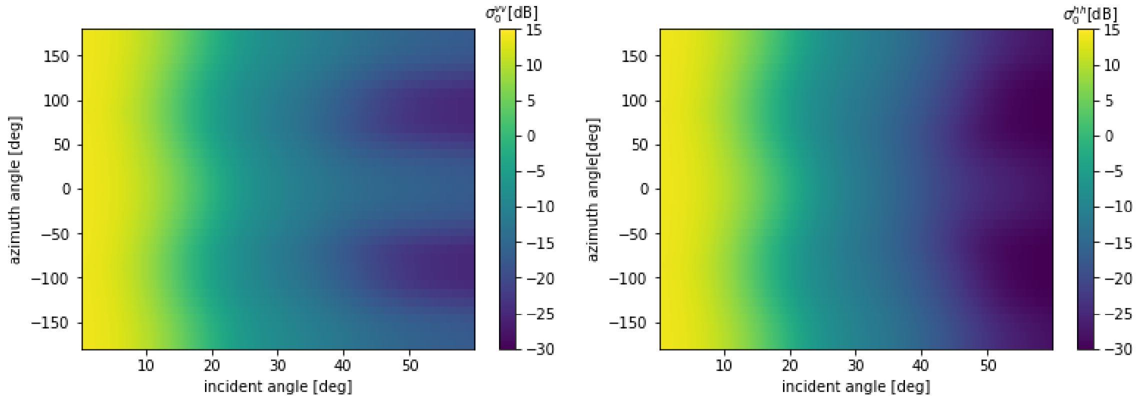

(a)

(b)

Figure 3.11: C-band total NRCS in fully-developed sea with wind speed $u_{10} = 10m/s$ condition for (a) vertical polarization and (b) horizontal polarization.

at different incident angles, figure 3.12 illustrates the NRCS at a single azimuth angle ($\varphi = 0$). At near-nadir incident angles ($< 15°$), specular reflection is dominated and compensates for the dips caused by the composite Bragg scattering models' invalidity. Bragg scattering gradually becomes the dominating source at moderate incident angles, while wave breaking contribution is relatively smaller as compared with it. But in horizontal polarization, Bragg scattering contribution is less than in vertical, therefore, wave breaking NRCS is relatively more significant.

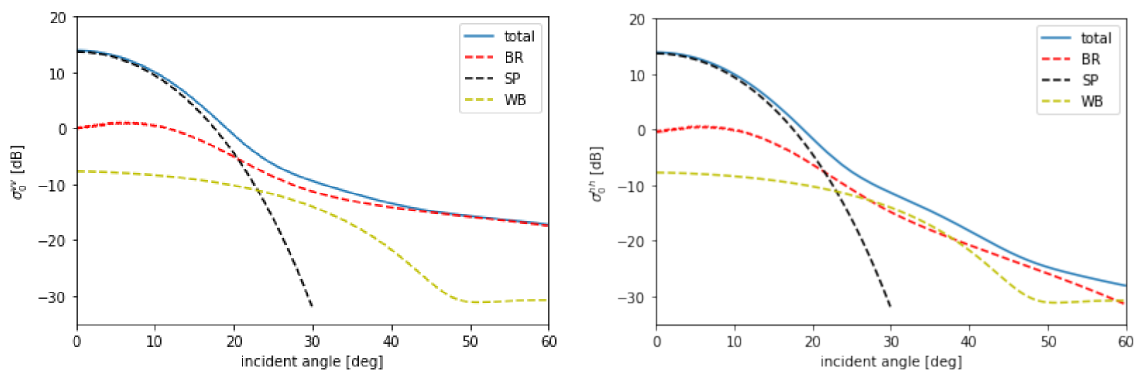

(a)

(b)

Figure 3.12: C-band total NRCS in fully-developed sea with wind speed $u_{10} = 10m/s$ condition for (a) vertical polarization and (b) horizontal polarization, when azimuth angle is zero.

The total NRCS for cross-polarization only contains Bragg scattering and wave breaking mechanisms, as these empirical models are validated from 20° incident angle where the contribution of specular reflection is negligible. Figure 3.13(a) illustrates the directional cross-polarization NRCS in C-band in a fully-developed sea with $10m/s$ wind speed, wave breaking contributes more to total NRCS in both crosswind and upwind directions as it compensates the small Bragg scattering NRCS there in figure 3.6. The NRCS in the downwind direction($\varphi = 0$) is shown in figure 3.13(b) to inspect the contributions of two mechanisms. At the small incident angles, Bragg scattering and wave breaking equally contribute to the total NRCS, whit the increase of incident angle, Bragg scattering contribution begins to play a more important role.

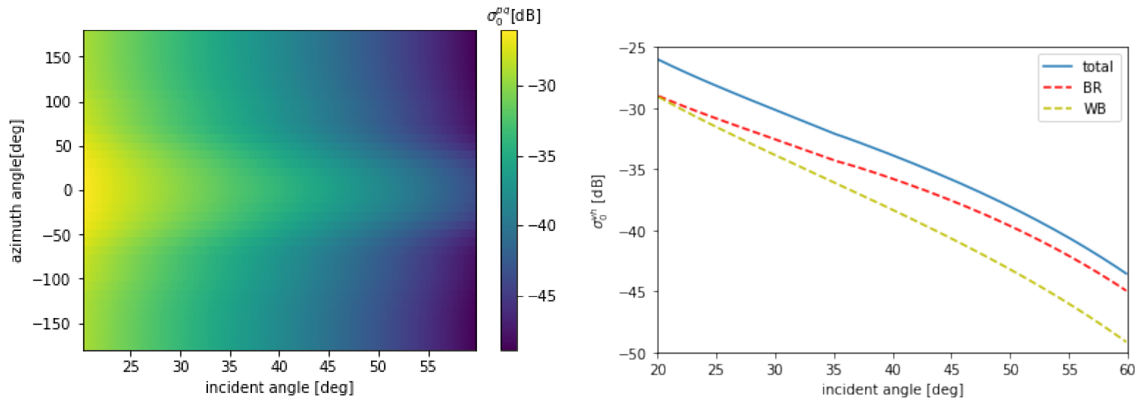

(a) (b)

Figure 3.13: Cross-polarization C-band total NRCS in fully-developed sea with wind speed $u_{10} = 10m/s$ condition. (a) Directional NRCS, (b) NRCS in the downwind direction.

3.5. Validation

A C-band geophysical model function CMOD5.N for equivalent neutral wind is regarded as measurements to validate the vertical polarization modeled results. From Hersbach [2010], this function provides an empirical relation between C-band backscatter as sensed by spaceborne European Remote Sensing Satellite-2 (ERS-2) and Advanced Scatterometers (ASCAT) and equivalent neutral ocean vector wind at 10-meter height as a function of incident angle. One of the two main disadvantages of this function is a mismatch between CMOD5.N and the backscatter measurements at low wind speeds, another is wind retrievals with CMOD5.N show wind speed probability distribution functions that depend on wind vector position across the swath, which is undesirable.

The validity of CMOD5.N. is from 17 to 66 degrees incident angles, and the results of validating the NRCS model with it for vertical polarization with $10m/s$ wind speed are illustrated in figure 3.14 in downwind, crosswind and upwind direction respectively. The model fits the measurements well in all directions, while they show different features. Besides the defects of the function itself, the main source of varying behaviors is the diverse wave spectrum expressions from equation (2.34) to (2.36). In the downwind direction, the model underestimates the measurements as the wave breaking energy source is ignored when deriving the spectrum. In the crosswind direction, the model underestimates for relatively small ($< 30°$) and large ($> 40°$) incident angles, while it overestimates at angles in between. This is caused by the simplification of assuming the wind growth rate as zero. In the upwind direction, the model overestimates the measurements from 30° because the wind input energy at upwind direction is overestimated.

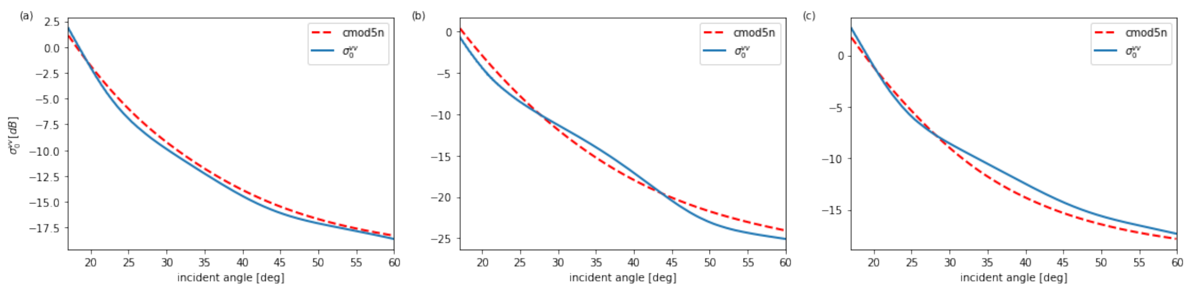

Figure 3.14: Validation with CMOD5.N. model for vertical polarization with $10m/s$ wind speed in (a) downwind $\varphi = 30°$ (b) crosswind $\varphi = 90°$ and (c) upwind direction $\varphi = 170°$.

3.6. Conclusion

Three different mechanisms, Bragg scattering, specular reflection, and wave breaking, are collaborated in constructing the mono-static backscatter model, equation (3.31), for different polarization states. For small incident angles, specular reflection is dominant, with the increase of incident angle, the other two mechanisms gradually take its place. Specular reflection and wave breaking mechanisms don't depend on polarization based on previous researches, while Bragg scattering slightly changes the expression because of different scattering coefficients. For co-polarization states, the models are built with statistical theories, while only empirical models are available for cross-polarization. The vertical co-polarized model shows significantly consistent with the CMOD.5N for all directions and will be applied to further upper ocean dynamics simulation in chapter 5.

4

Bistatic ocean backscatter model

The backscatter model in chapter 3 applies to mono-static radar, in which the transmitter and receiver are collocated. Conversely, bistatic radar uses antennas at separate platforms for transmission and reception. In this chapter, the first model to approximate bistatic NRCS that includes three mechanisms is provided. A conversion of the backscatter model from mono-static to bistatic geometry is applied based on Elfouhaily et al. [1999], and begin with an equivalent mono-static case derived from bistatic geometry. The final bistatic model is realized by scaling the equivalent mono-static model with polarization vectors which are oriented in different directions. The polarization vector depends on scattering mechanisms, here the orientation of the dominant Bragg scattering polarization vector is considered as the co-polarization in bistatic geometry, while specular reflection and wave breaking polarization vectors are rotated to it. Together with the co-polarized backscatter, signals received at polarization orthogonal to the co-polar, which is regarded as cross-polarization, are also considered.

4.1. Equivalent mono-static model

The equivalent mono-static system is defined by both equivalent geometry and equivalent wave number. Based on the same coordinate system as the mono-static geometry in figure 3.1, the simplified geometry of the bistatic system, comparable to the configuration of the Earth Explorer 10 candidate Harmony, is illustrated in figure 4.1. The transmitter and two receivers are represented by T, R_A, and R_B respectively. The two receivers are trailing and heading the transmitter and have therefore opposite bistatic angles, so only one receiver R_A is used to illustrate the theory. Point E between R_A and T is the hypothetical equivalent mono-static radar. Correspondingly, θ_i is the incident angle of the transmitter, θ_s is the scattering angle, and θ_{eq} is the equivalent mono-static incident angle. The angle between the azimuth direction of the incoming and scattering field is the bistatic angle ϕ_b. Assuming the transmitter always looks in the positive x-direction and the wind direction is defined with respect to the same direction, for equivalent mono-static radar E, the azimuth angle can be defined as

$$\varphi_{\text{eq}} = \varphi_w - \frac{\phi_b}{2}, \tag{4.1}$$

where φ_w is the wind direction. In this study, as transmission and reception satellites fly in the same orbit, the scattering angle, bistatic angle and equivalent mono-static angle can all be derived from the incident angle of the transmitter.

In the mono-static case, the incident wave number $\mathbf{k}_i$ and the scattered wave number $\mathbf{k}_s$ have the same magnitudes but oriented in opposite directions, thus the received wave number magnitudes in the mono-static case doesn't change. Analogically, the equivalent mono-static wave number $\mathbf{k}^{\text{eq}}$ can be defined as

$$\mathbf{k}^{\text{eq}} = \frac{\mathbf{k}_i - \mathbf{k}_s}{2}. \tag{4.2}$$

In this case, the incident and scattered wave numbers are not in the parallel direction but separated by an angle. As shown in the top view of the geometry in figure 4.2, the effective wavelength increases. Therefore, the magnitude of equivalent wave number k^{eq} can be computed by multiplying mono-static wave number k by $\cos\phi_b/2$, and it is written as

$$k^{\text{eq}} = k\cos\phi_b/2. \tag{4.3}$$

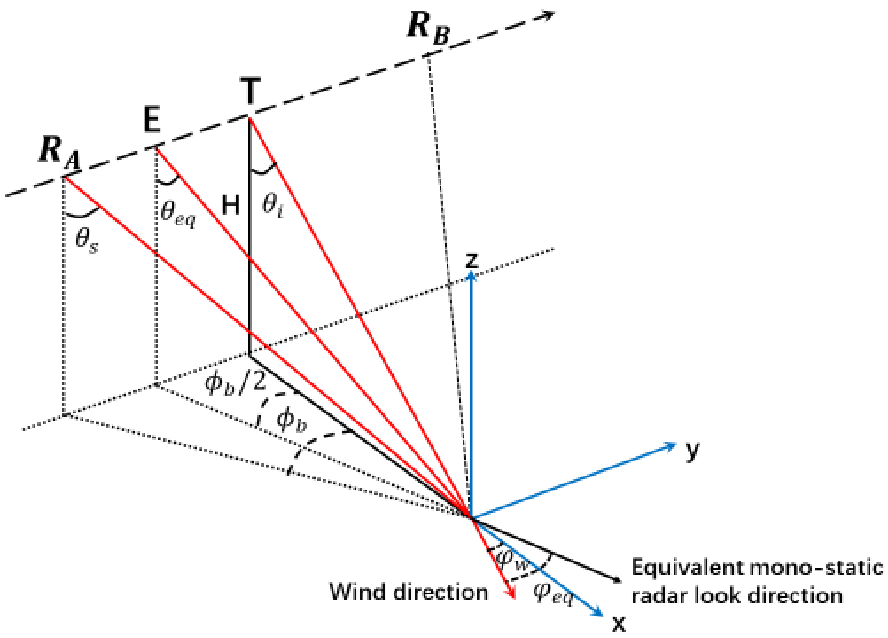

Figure 4.1: Bistatic geometry.

This wave number projection changes the local wave number of the Bragg waves, therefore changes the integral limits in the co-polarized composite Bragg model. Similar to equation (3.1), the co-polarized equivalent mono-static Bragg scattering model can be written as

$$\sigma_{Br}^{\mathrm{eq},pp}(\theta_{\mathrm{eq}},\varphi_{\mathrm{eq}}) = \int_\Gamma \sigma_{0\mathrm{Br}}^{\mathrm{eq},pp}(\theta'_{\mathrm{eq}},\varphi_{\mathrm{eq}})P(\eta_i)d\eta_i, \tag{4.4}$$

where $\theta'_{\mathrm{eq}} = \theta_{\mathrm{eq}} - \arctan\eta_i$ is the equivalent mono-static local incident angle. With the equivalent wave number defined in equation (4.3), the local wave number of the Bragg waves is

$$k_{\mathrm{Br}}^{\mathrm{eq}} = 2k_r \sin\theta'_{\mathrm{eq}} \cos(\phi_b/2). \tag{4.5}$$

Thus the integral limit Γ in equation (4.4) can be derived from the condition

$$2k_r \sin|\theta_{\mathrm{eq}} - \arctan\eta_i| \cos(\phi_b/2) \geq k_d, \tag{4.6}$$

as

$$\Gamma = \left[\eta_i \leq \tan(\theta_{\mathrm{eq}} - \frac{d}{2\cos(\phi_b/2)}) \cup \eta_i \geq \tan(\theta_{\mathrm{eq}} + \frac{d}{2\cos(\phi_b/2)})\right]. \tag{4.7}$$

For the cross-polarization state, changing the corresponding wave number and angles, the equation (3.11) in the equivalent mono-static case can be written as

$$\sigma_{\mathrm{Br}}^{\mathrm{eq},pq}(\theta_{\mathrm{eq}},\varphi_{\mathrm{eq}}) = \pi \tan^{-4}\theta_{\mathrm{eq}} |G_{pp} - G_{qq}|^2 \frac{s_{\mathrm{eq},n}^2}{\sin^2\theta_{\mathrm{eq}}} \times B(k_{\mathrm{Br}}^{\mathrm{eq}},\varphi_{\mathrm{eq}}), \tag{4.8}$$

where $s_{\mathrm{eq},n}^2 = 2.25 \times 10^{-3} \ln(\Omega_\alpha^{-2} k_d^{\mathrm{eq}} u_{10}^2/g)$ with $k_d^{\mathrm{eq}} = k_{\mathrm{Br}}^{\mathrm{eq}}/4$.

Changing the local wave number of Bragg waves also effects the specular reflection term when computing the mean square slopes in equation (3.18) and (3.19), while the wave breaking contribution is wave number independent. The equivalent mono-static model for specular reflection is

$$\sigma_{\mathrm{sp}}^{\mathrm{eq}}(\theta_{\mathrm{eq}},\varphi_{\mathrm{eq}}) = \pi |R_{xx}^{\mathrm{eq}}(\theta'_{\mathrm{eq}})|^2 \sec^4\theta_{\mathrm{eq}} \cdot P(\eta_i,\eta_n)|_{\eta_i=\tan\theta_{\mathrm{eq}},\eta_n=0}, \tag{4.9}$$

for co-polarized wave breaking is

$$\sigma_{\mathrm{wb}}^{\mathrm{eq},pp}(\theta_{\mathrm{eq}},\varphi_{\mathrm{eq}}) = \sigma_{0\mathrm{wb}}^{\mathrm{eq}}(\theta_{\mathrm{eq}}) \cdot (1 + M_{\mathrm{twb}}\overline{\theta_{\mathrm{wb}}}A_{\mathrm{wb}}(\varphi_{\mathrm{eq}})), \tag{4.10}$$

and for cross-polarized wave breaking is

$$\sigma_{\mathrm{wb}}^{\mathrm{eq},pq}(\theta_{\mathrm{eq}}) = \pi \frac{|G_{pp}(\theta_{\mathrm{eq}}) - G_{qq}(\theta_{\mathrm{eq}})|^2}{\tan^4\theta_{\mathrm{eq}}} \frac{s_{\mathrm{wb}}^2}{2\sin^2\theta_{\mathrm{eq}}} B_{\mathrm{wb}}. \tag{4.11}$$

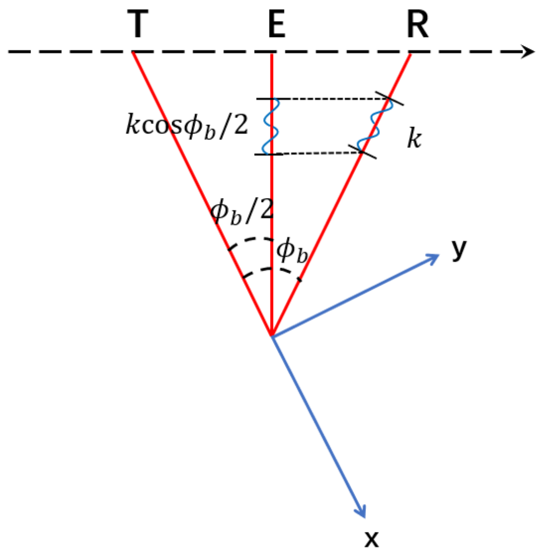

Figure 4.2: Top view of bistatic geometry.

4.2. Bistatic model

The Elfouhaily's bistatic model in Elfouhaily et al. [1999] applies to perfectly conducting surfaces, which exhibit infinite electrical conductivity. In this study, Elfouhaily's model is assumed valid for imperfect conducting surfaces and used to convert the equivalent mono-static model in the previous section to bistatic geometry. For this conversion procedure, the polarization vectors of the incident field $\mathbf{P}_i$, scattered field $\mathbf{P}_s$, receiver antenna $\mathbf{P}_r$, and their rotations have to be considered. The incident filed is given as an input, and the scattered field polarization vector is a function of $\mathbf{P}_i$, geometry, and scattering mechanism. To derive the scattered field $\mathbf{P}_s$, two iteration steps are included. The first-iteration field is known as the Kirchhoff field with polarization vector $\mathbf{P}_{s1}$, and the polarization rotation of it is defined with respect to the incident field as α_1. This field is an approximation for the Stratton-Chu's integral solution in Stratton [1983] for electric and magnetic fields, and it represents the scattering in a quasi-specular regime. Both specular reflection and wave breaking scattered fields are pure Kirchhoff fields, as their contributions are independent of polarization in mono-static co-polarization cases. The second-iteration gives the supplementary field with polarization vector $\mathbf{P}_{s2}$, its rotation to the incident field is represented by α_2. Adding two iteration processes together, we can get the total polarization vector $\mathbf{P}_s$ and total rotation angle α_s which is the field of dominant Bragg scattering. In this study, the bistatic model is built by scaling the equivalent mono-static model with the polarization vectors and rotating each field to the receive orientation.

For specular reflection and wave breaking mechanisms, their scattered fields are the Kirchhoff fields with the same polarization vector $\mathbf{P}_{s1}$, thus the transfer factor can be written as

$$M_1 = \frac{|\mathbf{P}_{s1}^{b}|^2}{|\mathbf{P}_{s1}^{\mathrm{eq}}|^2}, \tag{4.12}$$

where both $\mathbf{P}_{s1}^{b}$ and $\mathbf{P}_{s1}^{\mathrm{eq}}$ have the same transmit polarization. Therefore, the bistatic model before the rotation to the receiver direction for specular reflection is

$$\sigma_{\mathrm{sp}}^{\mathbf{P}_{s1}^{b},p}(\theta_{\mathrm{eq}},\varphi_{\mathrm{eq}}) = M_1\sigma_{\mathrm{sp}}^{\mathrm{eq}}(\theta_{\mathrm{eq}}), \tag{4.13}$$

and for wave breaking is

$$\sigma_{\mathrm{wb}}^{\mathbf{P}_{s1}^{b},p}(\varphi_{\mathrm{eq}},\theta_{\mathrm{eq}}) = M_1\sigma_{\mathrm{wb}}^{\mathrm{eq},pp}(\theta_{\mathrm{eq}}), \tag{4.14}$$

$$\sigma_{\mathrm{wb}}^{\mathbf{P}_{s1\perp}^{b},p}(\varphi_{\mathrm{eq}},\theta_{\mathrm{eq}}) = M_1\sigma_{\mathrm{wb}}^{\mathrm{eq},pq}(\theta_{\mathrm{eq}}), \tag{4.15}$$

where $\sigma_{\mathrm{wb}}^{\mathbf{P}_{s1}^{b},p}$ and $\sigma_{\mathrm{wb}}^{\mathbf{P}_{s1\perp}^{b},p}$ represent co- and cross-polarization wave breaking model respectively. For Bragg scattering, the polarization field is the scattered field with polarization vector $\mathbf{P}_s$, thus the transfer factor is

$$M_s = \frac{|\mathbf{P}_s^b|^2}{|\mathbf{P}_s^{\text{eq}}|^2}, \tag{4.16}$$

and the bistatic Bragg scattering model before the rotation to the receiver direction is

$$\sigma_{\text{Br}}^{\mathbf{P}_s^b,p}(\theta_{\text{eq}},\varphi_{\text{eq}}) = M_s\sigma_{\text{Br}}^{\text{eq},pp}(\theta_{\text{eq}}), \tag{4.17}$$

$$\sigma_{\text{Br}}^{\mathbf{P}_{s\perp}^b,p}(\theta_{\text{eq}},\varphi_{\text{eq}}) = M_s\sigma_{\text{Br}}^{\text{eq},pq}(\theta_{\text{eq}}), \tag{4.18}$$

where $\sigma_{\text{Br}}^{\mathbf{P}_s^b,p}$ and $\sigma_{\text{Br}}^{\mathbf{P}_{s\perp}^b,p}$ represent co- and cross-polarization Bragg scattering model respectively.

The assumed bistatic polarimetry profile is illustrated in figure 4.3, with $\mathbf{E}$ represents fields of different mechanisms. The scattered field $\mathbf{E}_s$ with polarization vector $\mathbf{P}_s$ is defined as the co-polar orientation in this study, while the field $\mathbf{E}_{s\perp}$ which is perpendicular to the scattered field is regarded as the cross-polarization. As the polarization vector is mechanism dependent, the co-polar non-Bragg scattering mechanisms con-

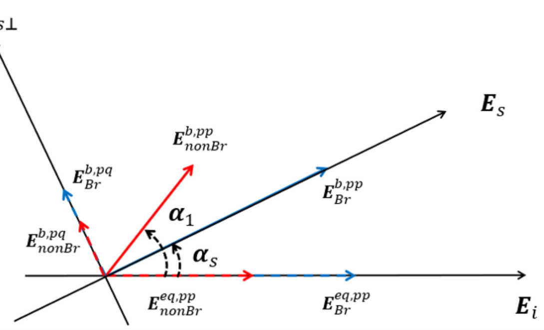

Figure 4.3: Bistatic polarimetry.

tribution to co- and cross-polarization total backscatter should be rotated to the orientation of $\mathbf{E}_s$ and $\mathbf{E}_{s\perp}$ respectively. With the Kirchhoff field orientation α_1 and the scattering field orientation α_s, the rotation angle with respect to the scattered field is defined as

$$\Delta\alpha = \alpha_1 - \alpha_s. \tag{4.19}$$

Hence, the total co-polar bistatic NRCS can be written as

$$\sigma_0^{\mathbf{P}_s^b,p} = \sigma_{\text{Br}}^{\mathbf{P}_s^b,p}(1-q) + [\sigma_{\text{sp}}^{\mathbf{P}_{s1}^b,p}(1-q) + \sigma_{\text{wb}}^{\mathbf{P}_{s1}^b,p}q]\cos^2\Delta\alpha. \tag{4.20}$$

For the total cross-polar bistatic backscatter, the rotation between non-Bragg and Bragg mechanism is ignored as their magnitudes are small. The cross-polarized model can be written as

$$\sigma_0^{\mathbf{P}_{s\perp}^b,p} = \sigma_{\text{Br}}^{\mathbf{P}_{s\perp}^b,p}(1-q) + \sigma_{\text{sp}}^{\mathbf{P}_{s1\perp}^b,p}(1-q) + \sigma_{\text{wb}}^{\mathbf{P}_{s1\perp}^b,p}q + [\sigma_{\text{sp}}^{\mathbf{P}_{s1}^b,p}(1-q) + \sigma_{\text{wb}}^{\mathbf{P}_{s1}^b,p}q]\sin^2\Delta\alpha. \tag{4.21}$$

4.3. Results

In order to illustrate the backscatter received in each satellite, a multi-static system is set up with three satellites flying in the same orbit and separated by 350 km in between. Combined with the mono-static model in chapter 3, the transmitter T in the bistatic system receives signals and behaves as a mono-static radar. The range of incident angles is from 20° to 45°. All the geometric angles computed from incident angle θ_i are shown in figure 4.4. Bistatic angle ϕ_b decreases with the increase of incident angle, while scattered and equivalent mono-static incident angle increase with it, and the magnitudes of these two angles increase with the distance away from the transmitter T. As the range of the incident angle in this system starts from 20° where the specular contribution is negligible, only the wave breaking contribution to non-Bragg mechanism is included.

The total C-band NRCS received under 10 m/s wind speed condition with different polarization states for each satellite is illustrated in figure 4.5. Figures from left to right represent the signals received at satellite R_A,

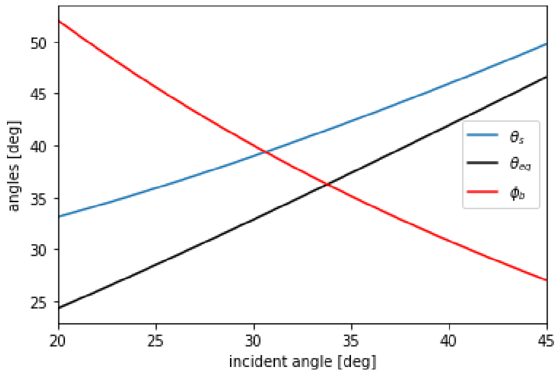

Figure 4.4: Angles in multi-static system.

T, and R_B respectively, and figures from top to the bottom represent the backscatter received at co-polar orientation with vertical incident polarization, co-polar orientation with horizontal incident polarization, and cross-polarization state respectively. The magnitudes of the received signals at each polarization show the same feature as the mono-static case in chapter 3, systems with vertical incident co-polarization received the most significant signals, while cross-polarization systems received signals are the least. Signals received in horizontal incident polarization state are slightly smaller than the vertical because of the effect of different geometric scattering features. The three figures in the middle, (b), (e), and (h), which represent the signals received at satellite T are all symmetric about the zero wind direction, while both side figures are shifted from the zero wind direction line. The axis of symmetry for both satellites R_A and R_B are bent because from equation (4.1) the equivalent azimuth angle is defined not only as a function of wind direction but also includes the effect of bistatic angle. The bistatic angle is a function of incident angle and it is defined positive all the time, thus the equivalent azimuth angle is $\varphi_w + \frac{\phi_b}{2}$ for satellite R_B. This explains why the R_A figures shift to positive wind direction and bend downward, while the R_B figures shift to negative wind direction and bend upward. For the cross-polarization case, both left and right sides figures, (g) and (i), show larger magnitudes than the middle one, especially for the directions outside the downwind range. This is caused by the assumptions made for the cross-polar bistatic scattering, where there are two parts of wave breaking contribution. One is the partly contribution from co-polar scattering because of the orientation of the scattered filed, another is the uniformly directional distributed cross-polar wave breaking contribution. Adding these two parts together, the crosswind and upwind received signals are enhanced for bistatic cross-polarization.

4.4. Conclusion

The bistatic backscatter models for co-polarization and cross-polarization are given in equation (4.20) and (4.21) respectively. For the co-polarized model, the orientation of the receiver antenna is assumed the same as the dominant Bragg scattering. For the cross-polarized model, the receiver antenna orientation is orthogonal to the co-polar. The magnitudes variation trend with different polarization is the same as the mono-static model, vertical co-polarization gives the maximum backscatter, followed by horizontal co-polarization, with the cross-polarization gives the least. For two receivers trailing (R_A) and heading (R_B) the transmitter (T) in the same orbit, the backscatter is different as their effective orientation with respect to the wind differs. The vertical co-polarized model will be applied to upper ocean dynamics simulation in chapter 5.

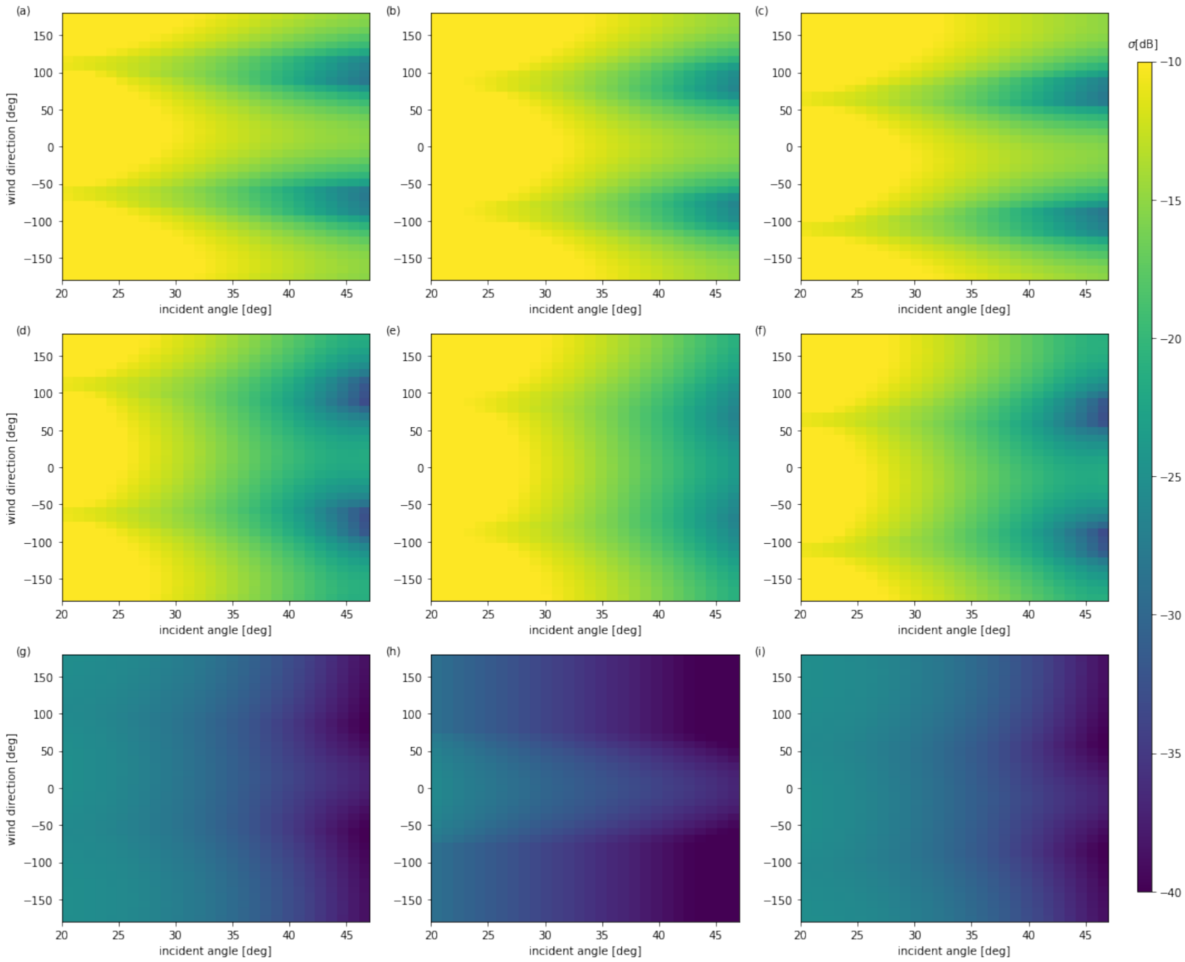

Figure 4.5: Multi-static C-band NRCS in fully-developed sea with wind speed u_{10} = 10 m/s condition. From left to right represents the signals received at satellite R_A, T and R_B respectively, from top to the bottom represents the backscatter received at vertical co-polarization, horizontal co-polarization and cross polarization state respectively.

5

Multi-static upper ocean dynamics simulation

In chapters 3 and 4, the backscatter models describe the background sea surface where the wind field is uniform and the surface currents are absent. In this chapter, the effect of non-uniform surface on the multi-static backscatter are simulated to manifest the ocean surface features. According to Kudryavtsev et al. [2005], two mechanisms are considered as the sources of nonuniformity in this study: the near-surface wind field and surface currents. These mechanisms act on the wind wave spectrum and thus modulate the NRCS. However, the modulated NRCS is relatively small and not clearly visible in radar images. For better visualization, the contrasts between short- and long-wave NRCS variations are computed, which are closely linked to changes in nonuniformity sources. To get a realistic modulation of the radar backscatter, the wind field and currents are derived from a coupled atmosphere-ocean model and Sentinel-3 Sea and Sand Surface Temperature Radiometer (SLSTR) obeservations. The modulation results are discussed and the simulation from Sentinel-3 measurements is qualitatively validated by comparing with the NRCS contrasts observed by the Sentinel-1 SAR instruments.

5.1. Wave spectrum modulation

In a nonuniform medium, the near-surface wind field and the surface current are the main contributors to the nonuniformity as suggested by Kudryavtsev et al. [2005]. The wave action spectrum $N(\mathbf{k})$ with considering these mechanisms is fully described by equation (2.16). The linearized equation with the variation in the energy source term $Q(\mathbf{k})$ and the dimensionless relaxation time, which describes the time required for the surface water to recover from shearing stress after the flow has ceased, the small spectrum modulations induced by the near-surface wind field and the surface current is presented in equation (44) of Kudryavtsev et al. [2005] as a transfer function $T(\mathbf{k})$ in Fourier space. For the surface current source, further researches in Johannessen et al. [2005] and Kudryavtsev et al. [2012] indicate that the current divergence is the only term that is retained after integration over the wind-wave directions. Therefore, the response of the wind-wave spectrum to the surface current is mainly governed by the divergence of the current field $\nabla \cdot \mathbf{u}$. Ignoring the directional effect, the simplified spectral transfer function T in physical space can be written as

$$T = c_\tau \frac{\hat{k}^{-3/2}}{1 + i \cdot c_\tau \hat{k}^{-2} \hat{K}} m_k (u_* / g) \nabla \cdot \mathbf{u}, \tag{5.1}$$

where $c_\tau = m_* / (2c_\beta)$ is a constant related to the wind growth parameter $c_\beta \approx 0.04$, while the wind exponent of spectrum m_* is estimated for waves longer and shorter than the wave at $k_{min} = 362$ rad/m separately by Trokhimovski and Irisov [2000]

$$m_* = \begin{cases} 1.1 \cdot k^{0.742} & k \le k_{min} \\ 5.61 - 1.19 \cdot k + 0.118 \cdot k^2 & k > k_{min} \end{cases}. \tag{5.2}$$

The dimensionless wave number of the wind waves and the Fourier component of the surface current are defined as $\hat{k} = k u_*^2 / g$ and $\hat{K} = K u_*^2 / g$, respectively. The wave number exponent of the omnidirectional spectrum of the wave action, $m_k = d \ln N / d \ln k$, is defined in Kudryavtsev et al. [2005]. Hence the modulated wave saturation spectrum in the physical space can be written as

$$B_m(\mathbf{k}) = B(\mathbf{k})(1 + |T|), \tag{5.3}$$

where $B(\mathbf{k})$ refers the saturation spectrum in equation (2.39) which is derived under background sea surface conditions. As the saturation spectrum is the base for the backscatter models in chapters 3 and 4, the modulation of the multi-static radar observables in a nonuniform medium can be applied.

5.2. Simulation from model

A coupled atmosphere-ocean model over California provides the near-surface wind field and the surface current velocity field with 1 km spatial resolution. The total wind velocity field is derived from a combination of the zonal wind velocity component U_w and the meridional wind velocity component V_w. The magnitude of the total wind velocity is written as

$$u_{10} = \sqrt{U_w^2 + V_w^2}, \tag{5.4}$$

and it is illustrated in figure 5.1(a). The wind direction with respect to the East is defined as

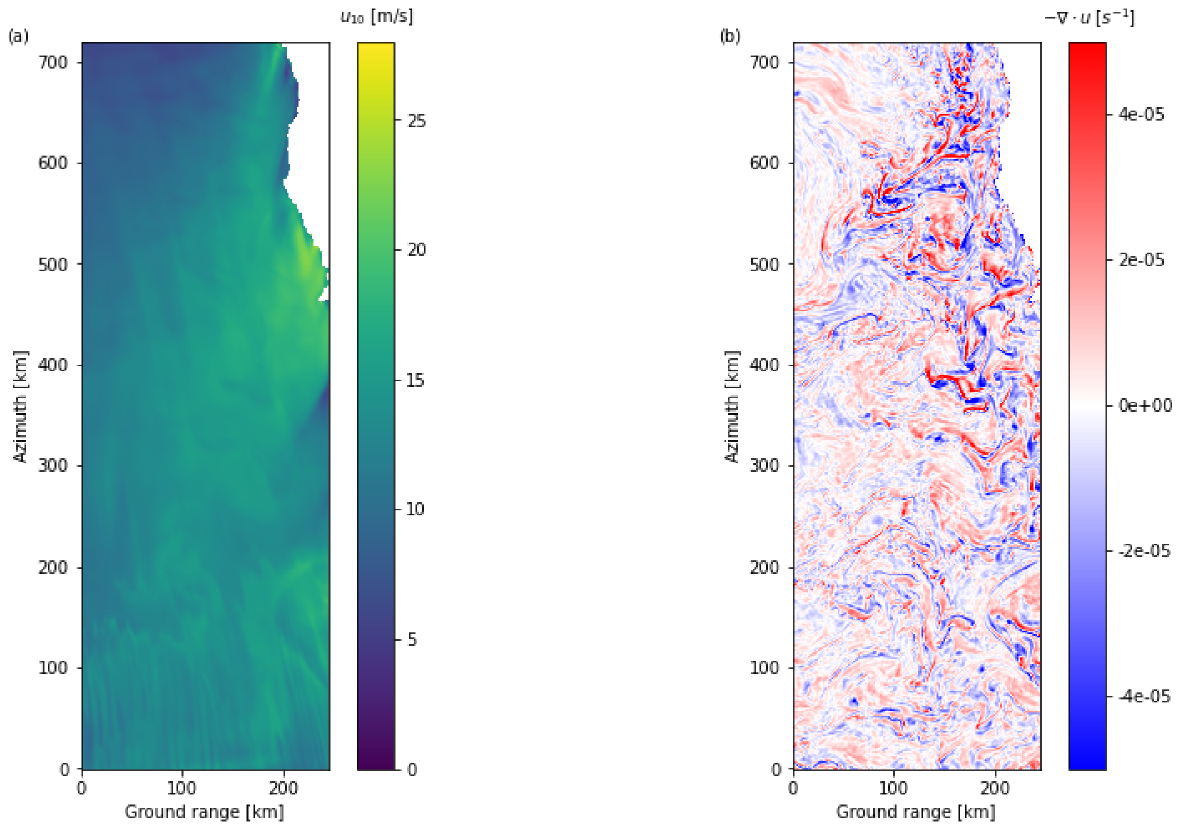

Figure 5.1: The coupled atmosphere-ocean model outputs over California: (a) the wind velocity magnitudes field and (b) the divergence of the current field.

$$\varphi_w = \arctan\left(\frac{V_w}{U_w}\right). \tag{5.5}$$

In this example, the computed mean wind direction is equal to $-70°$ and is used to better inspect the directional performance of the modulated models. From the current velocity components, the divergence of the current field can be derived as

$$\nabla \cdot \mathbf{u} = \frac{\partial U_c}{\partial x} + \frac{\partial V_c}{\partial y}, \tag{5.6}$$

where U_c and V_c are sea surface velocity components in the East and the North direction respectively. The inverted divergence field is illustrated in figure 5.1(b) and thus the red features correspond to the convergence zone and blue features correspond to the divergence zone.

A simulation is performed for a multi-static system of three satellites with one transmitter and three receivers, heading towards the North and looking toward the East is set. The system geometry, which is configured the same way as in chapter 4, is set with 350 km along-track separation and 31° near range incident angle which corresponds to the swath of the Interferometric Wide Swath mode of Sentinel-1.

The modulation of the NRCS by the surface currents and the near-surface wind field are almost invisible in the SAR images. Therefore contrasts between short- and long-wavelength signals in the NRCS images are computed. The NRCS contrasts magnify the manifestation of sea surface signatures in comparison to the original backscatter is used to represent the simulated results. It is defined as the ratio of high-pass and low-pass filtered NRCS, and can be written as

$$K_\sigma^m = (\sigma_0^m - \overline{\sigma_0^m})/\overline{\sigma_0^m}, \tag{5.7}$$

where σ_0^m is the modulated NRCS, and $\overline{\sigma_0^m}$ is the low-pass filtered modulated NRCS. In this case, $\overline{\sigma_0^m}$ is the average NRCS over a 5 km ×5 km window. The resulting NRCS contrasts images are shown in figure 5.2. From

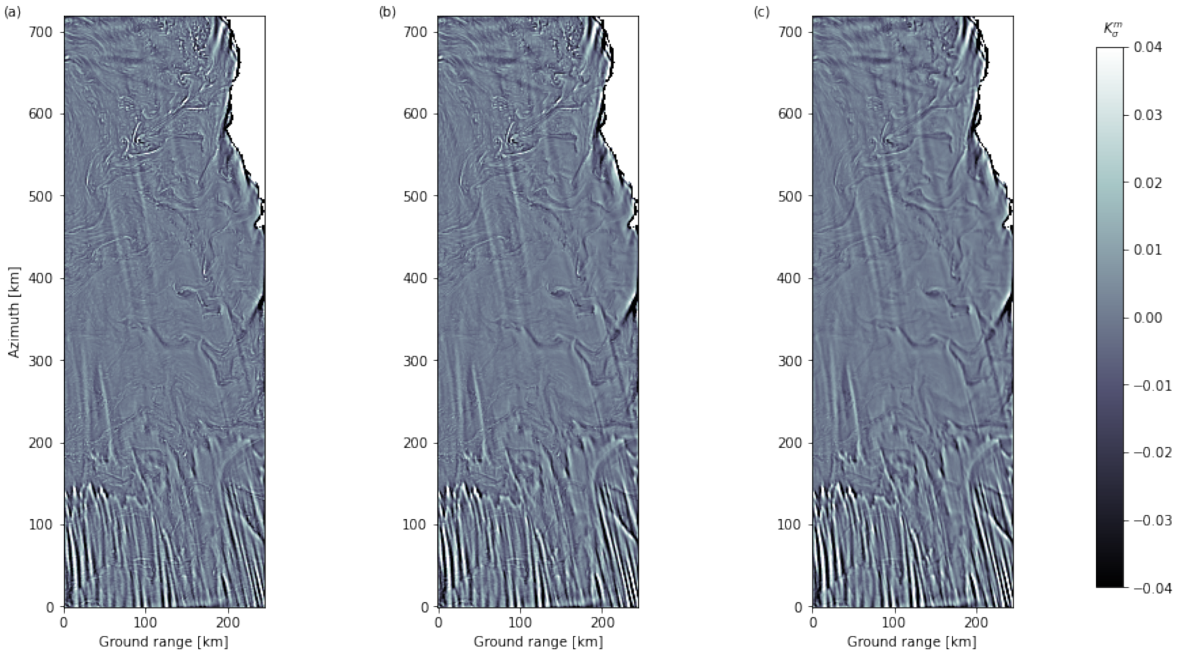

Figure 5.2: Multi-static C-band upper ocean dynamics backscatter simulations over California at the position of satellite (a) R_A, (b) T and (c) R_B respectively.

left to right, the images are simulations for satellite R_A, T, and R_B respectively. Both wind patterns and currents, which correspond to figure 5.1(a) and (b), leave significant traces in the NRCS contrasts images, but the discussion in this study will limit to ocean patterns. A comparison between figure 5.1 (b) and figure 5.2 reveals the correlation between the divergence and the NRCS contrasts, the positive/negative NRCS contrasts correspond to convergence/divergence of the surface currents. From figure 5.2 the NRCS modulation for each receiver varies, without considering the effect of polarization vectors' rotation in bistatic satellites, the main difference between these three simulations is the direction with respect to the wind. The left one for satellite R_A is the most sensitive to the small disturbances and shows detailed information of the current. For the mono-static radar T in the middle, the detailed information for the weak current around the azimuth range 250 km is less visible than that in the satellite R_A image. The satellite R_B gives the least current details, even for the strongest current around azimuth range 600 km. The wind direction is −70° with respect to the East, the radar look direction with respect to the wind is changing from the crosswind to downwind, left to right. Therefore, one can conclude the modulated model is more sensitive to the current in the crosswind direction, and the sensitivity is decreasing when approaching the downwind direction. For the wind patterns, the sensitivity towards the strip features caused by the wind are getting larger when the radar look direction is closer to the downwind direction, left to right. The clearest example is the strips at the land edge around azimuth range over 650 km. This directional change is consistent with the total NRCS changes in the background sea surface condition, as illustrated in figure 4.5.

5.3. Simulation from measurements

In this section, an attempt is made to inspect the model performance with optical remote sensing measurements. According to Kudryavtsev et al. [2005], the sea surface temperature (SST) field shows high correspondence with the SAR roughness anomalies. Based on the theory introduced in section 1.1, the Ekman transport mechanism causes the divergence together with the temperature gradients, including the diabatic mixing mechanism, the divergence can be derived from the Sentinel-3 SLSTR SST measurements and used to perform the modulation.

5.3.1. Research area

The Western Gulf of Mexico is chosen as a research area, considering the upper ocean dynamics and data availability. This is a highly dynamic area and the dynamics are dominated by the powerful northward Yucatan Current. This strong current flows into the basin and forms a warm loop, called the Loop Current that exits through the Florida Straits Counillon and Bertino [2009]. This Loop Current repeatedly sheds large scale (100- to 200-km diameter) anticyclonic rings Müller-Karger et al. [1991] which advect westwards Elliott [1982]. This process contributes to the abundant local ocean circulations inside the Western Gulf of Mexico basin and such upper ocean currents are routinely monitored via in-situ measurement method and satellite.

From the remote sensing aspect, the Western Gulf of Mexico has three essential advantages. Firstly, reduced cloud cover during the Northern hemisphere spring limits the contamination of SST data by clouds. Secondly, the temporal offset is relatively small (4 hours), such that temperature variations during these periods are limited. Lastly, abundant reduced atmosphere effect SAR images give more chance to find data with consistent ocean features in the SST measurements.

5.3.2. SST-derived divergence

The SST measurements with reduced cloud cover in the research area is illustrated in figure 5.3. A strong current with a cold core is present at the top of the figure, and a weak eddy is located in the middle of the bottom.

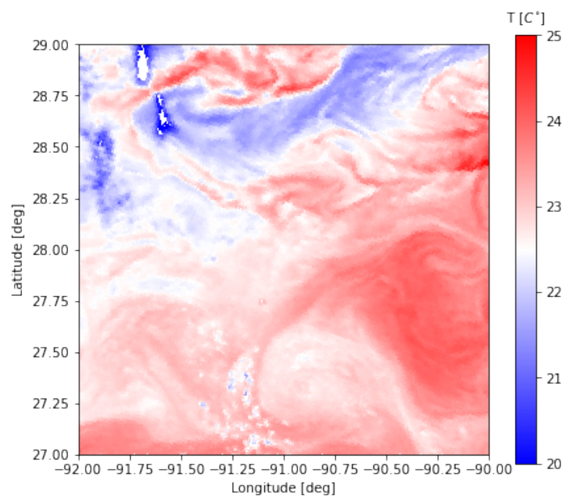

Figure 5.3: Sea surface temperature field derived from Sentinel-3 image with white spots represent masked clouds (11 April, 2019, 04:06 UTC).

According to Kudryavtsev et al. [2005], the divergence can be derived from the SST based on the Ekman transport and Ekman layer diabatic mixing mechanisms. To compute the divergence, the vorticity of the QGC field should be computed first. Vorticity as a characteristic of the kinematics of the flow describes the motion of the water. It is defined as the rotation of a fluid. From Poisson's equation, the vorticity of the QGC can be written as

$$\Omega = -\nabla^2 \psi, \tag{5.8}$$

where ∇^2 is the Laplace operator, and ψ is the stream function of the QGC field. The stream function is defined for incompressible flows and its derivative with respect to any direction would give the velocity component at right angles to that direction. Considering the surface quasi-geostrophic (SQG) dynamics, a practical approach for deriving the stream function from the SST field is proposed by Isern-Fontanet et al. [2008]. In the Fourier space, the stream function $\hat{\psi}(\mathbf{k}, z)$ and the SST field $\hat{T}_s(\mathbf{k})$ are linked by the relation

$$\hat{\psi}(\mathbf{k}, z) = \frac{g\alpha \hat{T}_s(\mathbf{k})}{f n_b k} e^{n_0 k z}, \tag{5.9}$$

where $\alpha = 207 \times 10^{-6} K^{-1}$ is the volumetric thermal expansion coefficient of water at $20°C$. The Brunt-Väisälä frequency N determines the Prandtl ratio $n = N/f$, here $n_0 = n_b = 50$ as assumed by Kudryavtsev et al. [2012]. The depth $z = 10\mu$m is where the sea surface temperature is measured. By combining equation (5.8) and equation (5.9), the vorticity derived from the SST data is computed, which is illustrated in figure 5.4. The vorticity field shows a variety of patterns and it traces even the weak temperature fronts within the eddy.

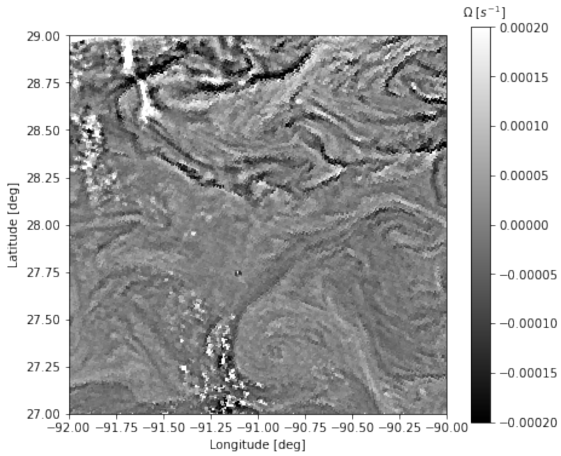

Figure 5.4: The vorticity of surface quasi-geostrophic current field derived from sea surface temperature.

In addition to the vorticity field, taking into account the interaction between Ekman flow and QGC, and thermal wind equation which represents the diabatic mixing mechanism in the Ekman layer. The divergence in the Fourier space reads

$$\widehat{\nabla \cdot u} = \frac{i\alpha}{\gamma_d^{1/4} n_b^{1/2}} \cdot \frac{g v_*}{f^2} \left[s \cdot \sin(\varphi_w - \varphi_K) + i \gamma_d^{3/4} n_b^{1/2} \frac{v_* K}{|f|} \right] K^2 \hat{T}_s, \tag{5.10}$$

where $\gamma_d = 0.2$ is a constant, $f = 10^{-4} s^{-1}$ is the approximated Coriolis coefficient. The sign of Coriolis parameter, $s = sign(f)$, is positive in northern hemisphere and negative in south hemisphere, φ_w is the wind direction vector, φ_K is the direction of wave number vector $\mathbf{K}$, $K = |\mathbf{K}|$. The friction velocity in the water v_* is defined as

$$v_* = \sqrt{\frac{\tau}{\rho_w}} \tag{5.11}$$

for general cases with $\tau = \rho_a C_D u_{10}^2$. To show the consistence with the more clear, the magnitude of derived divergence is inverted and illustrated in figure 5.5, the convergence/divergence patterns trace the gradients of vorticity field.

5.3.3. Simulations

Based on the wind measurements at the acquisition time of the Sentinel-3 data set, the wind input for the simulation is blowing northerly with 5 m/s mean speed. The multi-static observation geometry for the Western Gulf of Mexico is set the same as in section 5.2 and the simulation results are illustrated with the NRCS contrasts computed from equation (5.7). Here, the low-pass filtered modulated NRCS is averaged over the 30 km × 30 km window and the NRCS contrasts images are illustrated in figure 5.6 which only contain ocean surface signatures due to currents. From left to right, the images are simulations for satellite R_A, T, and R_B respectively. These images are too noisy to see the sensitivity of the current changes with the relative azimuth direction and details of the currents, but all of them do show the current signatures. The positive/negative

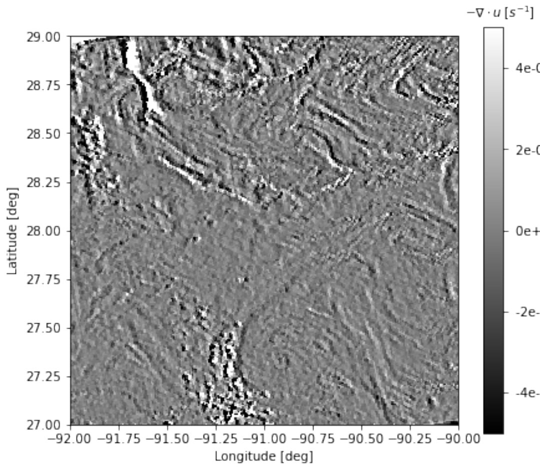

Figure 5.5: The inverted divergence of current field.

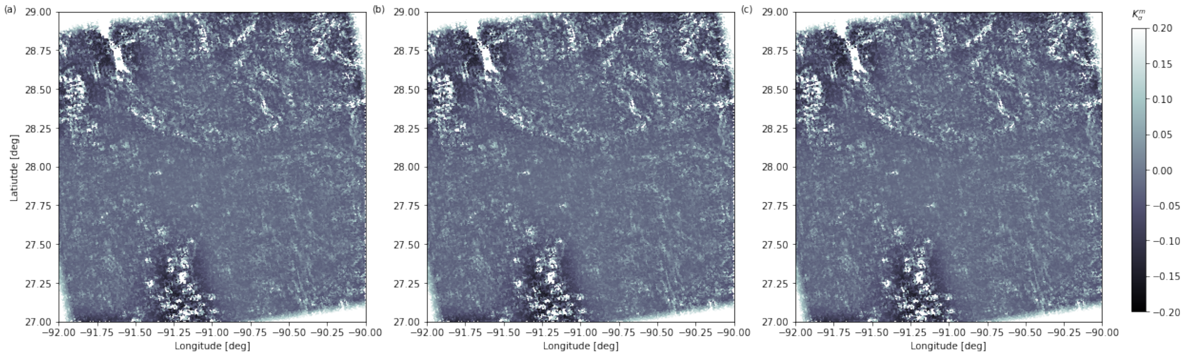

Figure 5.6: Multi-static C-band upper ocean dynamics backscatter simulations over the Western Gulf of Mexico at the position of satellite (a) R_A, (b) T and (c) R_B respectively.

NRCS contrasts correspond to convergence/divergence of the surface currents in figure 5.5, except the positive spots caused by the clouds. The outline of the upper cold-core current with strong temperature gradients is clearly shown in the NRCS contrasts patterns, while the eddy in the south with weak temperature gradients is fuzzy in all the simulations.

A Sentinel-1 SAR amplitude data set which shows similar upper ocean surface signatures with the SST measurements and covers the research area is used to inspect the performance of the simulations. The NRCS contrasts pattern of this SAR data set is constructed in the same way as the simulations from the optical measurements and shown in figure 5.7. As the acquisition time difference between SAR and optical data sets is about four hours, and the currents change during this period time, the current features in the two data sets are not identical. In the SAR contrasts pattern, the cold-core current in the north and the eddy in the south are visible, but the eddy pattern is contaminated. Focusing on the current in the north and comparing with the simulations in figure 5.6, the overall magnitude scale to illustrate the contrasts are the same and the bright outlines of the current in both figures trace the convergence zone in figure 5.5, thus the simulated results are qualitatively validated in this study.

5.4. Conclusion

Both the near-surface wind field and the surface currents contribute to modulate the multi-static radar observables, and their modulation performance changes with the observation direction of the satellite. The observed wind pattern magnitudes are larger in the downwind direction than in the crosswind direction. For the currents, the satellite in the crosswind direction is more sensitive to the current signatures, while the sensitivity decreases when the observation direction is closer to the downwind direction.

Considering the surface currents effect only, the modeled backscatter from the optical SST measurements

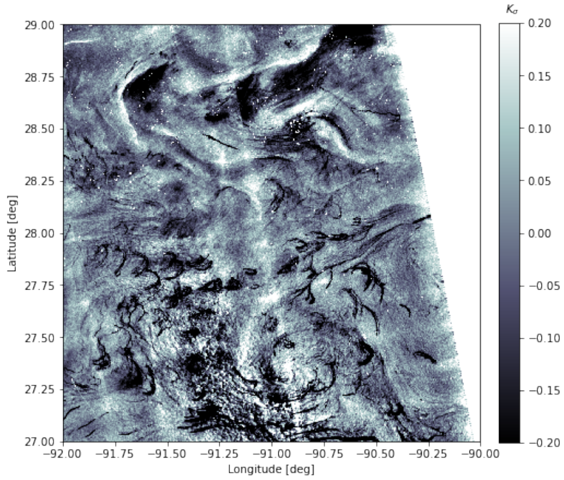

Figure 5.7: The radar observables from Sentinel-1 image (11 April, 2019, 00:10 UTC).

is qualitatively validated with the SAR observables in the overall magnitudes scale and the spatial distribution of convergence zone aspects. Three main factors contribute to the differences in the images. Firstly, the sea surface temperature is considered as the only source which contributes to the divergence, other dynamic processes like wind and salinity which would contribute to the surface signatures are excluded. Therefore, the pattern of the simulated results is an approximated sea surface that shows only the sea surface temperature related signatures. Moreover, the simulated signatures heavily rely on the strength of the temperature gradients, currents with weak temperature gradients are not visible in the simulations. Secondly, during the acquisition time difference between these two data sets, the temperature fronts change and thus change the scale of the structures and cause the shift of the divergence/convergence zones. Thirdly, the less quantity and the lower resolution of the sea surface features exhibit in the simulation indicate that the radar is much more sensitive to the surface features than the optical sensing instruments.

6

Conclusions and recommendations

6.1. Conclusions

In this study, the research question, *how do surface features modulate the multi-static radar signatures of the ocean surface*, is answered by covering three sub-questions proposed in section 1.3. The first sub-question is answered in chapter 2, by analytically describing wave spectra that are suitable to use for backscatter models. The second sub-question is addressed in chapters 3 and 4, where a bistatic ocean backscatter model is derived based on an ocean wave spectrum. The third sub-questions is answered in chapter 5 where the modulation of backscatter by surface currents, which are derived from the Sentinel-3 Sea and Land Surface Temperature Radiometer (SLSTR) sea surface temperature measurements. Those simulations over the Western Gulf of Mexico are qualitatively validated with Sentinel-3 synthetic aperture radar (SAR) measurements.

- How to represent the wave spectrum over the range of wave numbers that are relevant to radar observations?

  The curvature spectrum, which is validated from the spectral peak up to gravity-capillary peak wave number range, is constructed by considering the microwave measurements are modeled by waves with different scales. This wave spectrum consists of two spectral regimes. The long-wave curvature spectrum corresponds to the energy-containing range, is empirically derived from in-situ or tank measurements. The short-wave curvature spectrum correspond to equilibrium range, is derived from energy balance equation with the assumptions that the wind is steady and no currents present.

- How to model backscatter for mono-static SAR and convert it to a bistatic system?

  Three different mechanisms, Bragg scattering, specular reflection, and wave breaking, are considered in constructing a mono-static backscatter model. Specular reflection is dominant when incident angles are smaller than 20°, the other two mechanisms gradually increase as the incident angle increases. Specular reflection and wave breaking mechanisms' contributions do not depend on the polarization of the incident wave, while Bragg scattering slightly changes because of different scattering coefficients. Combine these three mechanisms, the total backscatter is larger in the downwind and upwind direction, while it is smaller in the crosswind direction. For co-polarization backscatter, the models are based on statistical theories, while only empirical models are available for cross-polarization.

  The bistatic backscatter is approximated with an equivalent mono-static system that is located in the middle of the transmitter and the receiver. The polarization changes are accounted for by a rotation that depends on the bistatic angle. The rotation of all three scattering mechanisms is different, but the reference polarization is taken in such a way that Bragg scattering only contributes to the co-polarization channel. Specular and wave breaking scatter have therefore contributions to both the co-polarization and cross-polarization. For two receivers trailing and heading the transmitter in the same orbit, the backscatter is different as their effective orientation with respect to the wind differs.

- How do current features modulate the wave spectrum, and how do these translate to a modulation of the multi-static NRCS?

  The surface currents contribute to modulate the multi-static radar observables by altering the waves. A transfer function is used to apply this alteration to the wave spectrum. The modulation changes with the effective observation direction of the transmitter-receiver system. In the crosswind direction, the satellite is more sensitive to the current signatures, while the sensitivity is smallest when the observation direction is in the downwind direction. The method to modulate backscatter has been demonstrated over the Western Gulf of Mexico, with the use of SST-derived currents. The results have been qualitatively validated using data from an overpass of the Sentinel-1 SAR satellite.

6.2. Recommendations

The results in this study might further be improved, hence several recommendations are made for further research. The recommendations are listed for each research chapter as follows:

- *The full wave number range wave spectrum of wind waves in chapter 2*
  - The spectrum of the long-waves is established with empirical relations derived from in-situ or tank measurements. Combining satellite radar altimetry measurements with SAR alows long-wave spectrum to be better understood and characterized.
- *The mono-static backscatter model for all polarization states in chapter 3*
  - Only the performance of the vertical co-polarization mono-static model with medium wind speed is validated insofar as the C-band geophysical model function (CMOD5.N) provides. The validation of the model for other polarization states could be made with other data sources.
- *The application of the mono-static model to bistatic geometry in chapter 4*
  - The geometry of the bistatic receivers are approximated symmetric around the transmitter and thus the only difference in geometry is the azimuth angle. To be more accurate, each receiver should have a specific geometry, accounting for the attitude laws of the satellites, which in turn are designed to compensate the rotation of the Earth.
  - The definition of the co-polarization states in the bistatic system based on the assumption that the orientation of the receiver antenna is the same as the dominant Bragg scattering. In general, the receiver not always locates in the optimal direction, thus the rotation of receiver antenna with respect to the dominant Bragg scattering field should be addressed.
- *Modulate the multi-static radar observables by current features in chapter 5*
  - The sensitivity to surface signatures changes with the direction, a directional expression for transfer function which is supposed to minimize the differences should be proposed.
  - Selecting the optical and SAR data-pair, which shows the same sea surface signatures, is a time -consuming work. A machine learning algorithm with specific training data sets considering the cloud cover, acquisition time difference and similarity of detected features should be proposed to make this process more efficient.
  - The visible sea surface features in the simulations with divergence derived from sea surface temperature heavily rely on the strength of the temperature gradient. And there could be cases where temperature fronts present but no radar detectable features. Therefore, the contribution of SST to radar observables should be further studied and other sea water properties should be included in deriving the divergence.

Bibliography

Werner Alpers. Ocean surface wave imaging from seasat to envisat. In *IGARSS 2003. 2003 IEEE International Geoscience and Remote Sensing Symposium. Proceedings (IEEE Cat. No. 03CH37477)*, volume 1, pages 35–37. IEEE, 2003.

Werner Alpers and Ingo Hennings. A theory of the imaging mechanism of underwater bottom topography by real and synthetic aperture radar. *Journal of Geophysical Research: Oceans*, 89(C6):10529–10546, 1984.

ML Banner, Ian SF Jones, and JC Trinder. Wavenumber spectra of short gravity waves. *Journal of Fluid Mechanics*, 198:321–344, 1989.

Josef Barthel, K Bachhuber, Richard Buchner, H Hetzenauer, and M Kleebauer. A computer-controlled system of transmission lines for the determination of the complex permittivity of lossy liquids between 8.5 and 90 ghz. *Berichte der Bunsengesellschaft für physikalische Chemie*, 95(8):853–859, 1991.

F Bass, I Fuks, A Kalmykov, I Ostrovsky, and A Rosenberg. Very high frequency radiowave scattering by a disturbed sea surface part i: Scattering from a slightly disturbed boundary. *IEEE Transactions on Antennas and Propagation*, 16(5):554–559, 1968.

Valentina Boccia, Erik De Witte, Josep Roselló, Michel Tossaint, Craig J Donlon, Klaus Scipal, Geoff Burbidge, Harald Johnsen, Franco Fois, Geir Engen, et al. Stereosar: A multi-static sar mission concept to enhance sentinel-1 capabilities for measuring ocean dynamics. In *Sensors, Systems, and Next-Generation Satellites XXI*, volume 10423, page 104230A. International Society for Optics and Photonics, 2017.

François Counillon and Laurent Bertino. High-resolution ensemble forecasting for the gulf of mexico eddies and fronts. *Ocean Dynamics*, 59(1):83–95, 2009.

Charles Cox and Walter Munk. Measurement of the roughness of the sea surface from photographs of the sun's glitter. *Josa*, 44(11):838–850, 1954.

Mark A Donelan, J Hamilton, and W_H Hui. Directional spectra of wind-generated ocean waves. *Philosophical Transactions of the Royal Society of London. Series A, Mathematical and Physical Sciences*, 315(1534): 509–562, 1985.

Tanos Elfouhaily, Bertrand Chapron, Kristina Katsaros, and Douglas Vandemark. A unified directional spectrum for long and short wind-driven waves. *Journal of Geophysical Research: Oceans*, 102(C7):15781–15796, 1997.

Tanos Elfouhaily, Donald R Thompson, Douglas Vandemark, and Bertrand Chapron. A new bistatic model for electromagnetic scattering from perfectly conducting random surfaces. *Waves in Random Media*, 9(3): 281–294, 1999.

Brady A Elliott. Anticyclonic rings in the gulf of mexico. *Journal of Physical Oceanography*, 12(11):1292–1309, 1982.

Eric A Ericson, David R Lyzenga, and David T Walker. Radar backscatter from stationary breaking waves. *Journal of Geophysical Research: Oceans*, 104(C12):29679–29695, 1999.

Christopher John Raymond Garrett and JW Loder. Dynamical aspects of shallow sea fronts. *Philosophical Transactions of the Royal Society of London. Series A, Mathematical and Physical Sciences*, 302(1472):563–581, 1981.

Tetsu Hara, Erik J Bock, and David Lyzenga. In situ measurements of capillary-gravity wave spectra using a scanning laser slope gauge and microwave radars. *Journal of Geophysical Research: Oceans*, 99(C6):12593–12602, 1994.

Klaus Hasselmann, TP Barnett, E Bouws, H Carlson, DE Cartwright, K Enke, JA Ewing, H Gienapp, DE Hasselmann, P Kruseman, et al. Measurements of wind-wave growth and swell decay during the joint north sea wave project (jonswap). *Ergänzungsheft 8-12*, 1973.

Hans Hersbach. Comparison of c-band scatterometer cmod5. n equivalent neutral winds with ecmwf. *Journal of Atmospheric and Oceanic Technology*, 27(4):721–736, 2010.

Leo H Holthuijsen. *Waves in oceanic and coastal waters.* Cambridge university press, 2010.

Jochen Horstmann, Wolfgang Koch, Susanne Lehner, and Rasmus Tonboe. Wind retrieval over the ocean using synthetic aperture radar with c-band hh polarization. *IEEE transactions on Geoscience and Remote sensing*, 38(5):2122–2131, 2000.

Paul A Hwang. A note on the ocean surface roughness spectrum. *Journal of Atmospheric and Oceanic Technology*, 28(3):436–443, 2011.

Jordi Isern-Fontanet, Guillaume Lapeyre, Patrice Klein, Bertrand Chapron, and Matthew W Hecht. Three-dimensional reconstruction of oceanic mesoscale currents from surface information. *Journal of Geophysical Research: Oceans*, 113(C9), 2008.

Bernd Jähne and Klaus S Riemer. Two-dimensional wave number spectra of small-scale water surface waves. *Journal of Geophysical Research: Oceans*, 95(C7):11531–11546, 1990.

Johnny A Johannessen, Vladimir Kudryavtsev, D Akimov, Tor Eldevik, N Winther, and B Chapron. On radar imaging of current features: 2. mesoscale eddy and current front detection. *Journal of Geophysical Research: Oceans*, 110(C7), 2005.

W Linwood Jones and LC Schroeder. Radar backscatter from the ocean: Dependence on surface friction velocity. *Boundary-Layer Meteorology*, 13(1-4):133–149, 1978.

WC Keller and JW Wright. Microwave scattering and the straining of wind-generated waves. *Radio Science*, 10(2):139–147, 1975.

Sergei Aleksandrovich Kitaigorodskii. The physics of air-sea interaction. 1973.

Patrice Klein and Bach Lien Hua. The mesoscale variability of the sea surface temperature: An analytical and numerical model. *Journal of Marine Research*, 48(4):729–763, 1990.

Vladimir Kudryavtsev and Johnny Johannessen. On effect of wave breaking on short wind waves. *Geophysical research letters*, 31(20), 2004.

Vladimir Kudryavtsev, Danièle Hauser, Gérard Caudal, and Bertrand Chapron. A semiempirical model of the normalized radar cross-section of the sea surface 1. background model. *Journal of Geophysical Research: Oceans*, 108(C3):FET–2, 2003.

Vladimir Kudryavtsev, D Akimov, Johnny Johannessen, and Bertrand Chapron. On radar imaging of current features: 1. model and comparison with observations. *Journal of Geophysical Research: Oceans*, 110(C7), 2005.

Vladimir Kudryavtsev, Alexander Myasoedov, Bertrand Chapron, Johnny A Johannessen, and Fabrice Collard. Imaging mesoscale upper ocean dynamics using synthetic aperture radar and optical data. *Journal of Geophysical Research: Oceans*, 117(C4), 2012.

Vladimir N Kudryavtsev, Shengren Fan, Biao Zhang, Alexis A Mouche, and Bertrand Chapron. On quad-polarized sar measurements of the ocean surface. *IEEE Transactions on Geoscience and Remote Sensing*, 57 (11):8362–8370, 2019.

VN Kudryavtsev, VK Makin, and Bertrand Chapron. Coupled sea surface-atmosphere model: 2. spectrum of short wind waves. *Journal of Geophysical Research: Oceans*, 104(C4):7625–7639, 1999.

Frank Lees. *Lees' Loss prevention in the process industries: Hazard identification, assessment and control.* Butterworth-Heinemann, 2012.

Susanne Lehner, Johannes Schulz-Stellenfleth, B Schattler, Helko Breit, and Jochen Horstmann. Wind and wave measurements using complex ers-2 sar wave mode data. *IEEE Transactions on Geoscience and Remote Sensing*, 38(5):2246–2257, 2000.

IA Leykin, KV Pokazeyev, and AD Rozenberg. Growth and saturation of wind waves in a laboratory channel. *Izv. Akad. Nauk SSSR, Fiz. Atmosf. Okean*, 20:297–304, 1984.

Paco López-Dekker, Helmut Rott, Pau Prats-Iraola, Bertrand Chapron, Klaus Scipal, and Erik De Witte. Harmony: An earth explorer 10 mission candidate to observe land, ice, and ocean surface dynamics. In *IGARSS 2019-2019 IEEE International Geoscience and Remote Sensing Symposium*, pages 8381–8384. IEEE, 2019.

DR Lyzenga. Effects of wave breaking on sar signatures observed near the edge of the gulf stream. In *IGARSS'96. 1996 International Geoscience and Remote Sensing Symposium*, volume 2, pages 908–910. IEEE, 1996.

Cornelis Mastenbroek. Wind-wave interaction. 1996.

Harunobu Masuko, Ken'ichi Okamoto, Masanobu Shimada, and Shuntaro Niwa. Measurement of microwave backscattering signatures of the ocean surface using x band and ka band airborne scatterometers. *Journal of Geophysical Research: Oceans*, 91(C11):13065–13083, 1986.

Alberto Moreira. A golden age for spaceborne sar systems. In *2014 20th International Conference on Microwaves, Radar and Wireless Communications (MIKON)*, pages 1–4. IEEE, 2014.

Alexis Mouche and Bertrand Chapron. Global c-b and e nvisat, radarsat-2 and s entinel-1 sar measurements in copolarization and cross-polarization. *Journal of Geophysical Research: Oceans*, 120(11):7195–7207, 2015.

Frank E Müller-Karger, John J Walsh, Robert H Evans, and Mark B Meyers. On the seasonal phytoplankton concentration and sea surface temperature cycles of the gulf of mexico as determined by satellites. *Journal of Geophysical Research: Oceans*, 96(C7):12645–12665, 1991.

Oliver M Phillips. The equilibrium range in the spectrum of wind-generated waves. *Journal of Fluid Mechanics*, 4(4):426–434, 1958.

OM Phillips. Spectral and statistical properties of the equilibrium range in wind-generated gravity waves. *Journal of Fluid Mechanics*, 156:505–531, 1985.

Owen M Phillips. *The dynamics of the upper ocean.* Cambridge university press, 1966.

Willard J Pierson Jr and Lionel Moskowitz. A proposed spectral form for fully developed wind seas based on the similarity theory of sa kitaigorodskii. *Journal of geophysical research*, 69(24):5181–5190, 1964.

William J Plant. Bragg scattering of electromagnetic waves from the air/sea interface. In *Surface waves and fluxes*, pages 41–108. Springer, 1990.

Y Quilfen, B Chapron, A Bentamy, J Gourrion, T El Fouhaily, and D Vandemark. Global ers 1 and 2 and nscat observations: Upwind/crosswind and upwind/downwind measurements. *Journal of Geophysical Research: Oceans*, 104(C5):11459–11469, 1999.

Roland Romeiser, Werner Alpers, and Volkmar Wismann. An improved composite surface model for the radar backscattering cross section of the ocean surface: 1. theory of the model and optimization/validation by scatterometer data. *Journal of Geophysical Research: Oceans*, 102(C11):25237–25250, 1997.

Stuart D Smith. Coefficients for sea surface wind stress, heat flux, and wind profiles as a function of wind speed and temperature. *Journal of Geophysical Research: Oceans*, 93(C12):15467–15472, 1988.

RW Stewart. The air-sea momentum exchange. *Boundary-Layer Meteorology*, 6(1-2):151–167, 1974.

JA Stratton. Electromagnetic theory (mcgraw-hill, new york, 1941). *There is no corresponding record for this reference.[Google Scholar]*, 1983.

DR Thompson. Calculation of radar backscatter modulations from internal waves. *Journal of Geophysical Research: Oceans*, 93(C10):12371–12380, 1988.

Yuri G Trokhimovski and Vladimir G Irisov. The analysis of wind exponents retrieved from microwave radar and radiometric measurements. *IEEE transactions on geoscience and remote sensing*, 38(1):470–479, 2000.

Christine MH Unal, Paul Snoeij, and Peter JF Swart. The polarization-dependent relation between radar backscatter from the ocean surface and surface wind vector at frequencies between 1 and 18 ghz. *IEEE transactions on Geoscience and Remote Sensing*, 29(4):621–626, 1991.

Gaspar R Valenzuela. Theories for the interaction of electromagnetic and oceanic waves—a review. *Boundary-Layer Meteorology*, 13(1-4):61–85, 1978.

DT Walker, DR Lyzenga, EA Ericson, and DE Lund. Radar backscatter and surface roughness measurements for stationary breaking waves. *Proceedings of the Royal Society of London. Series A: Mathematical, Physical and Engineering Sciences*, 452(1952):1953–1984, 1996.

Lewis Wetzel. On microwave scattering by breaking waves. In *Wave dynamics and radio probing of the ocean surface*, pages 273–284. Springer, 1986.

Lewis B Wetzel. Electromagnetic scattering from the sea at low grazing angles. In *Surface waves and fluxes*, pages 109–171. Springer, 1990.

Christian Wolff. Radartutorial. eu. *Retrieved May*, 3:2013, 2012.

Iain H Woodhouse. *Introduction to microwave remote sensing*. CRC press, 2005.

JW Wright. A new model for sea clutter. *IEEE Transactions on antennas and propagation*, 16(2):217–223, 1968.

Jin Wu. Wind-stress coefficients over sea surface near neutral conditions—a revisit. *Journal of Physical Oceanography*, 10(5):727–740, 1980.

MV Yurovskaya, VA Dulov, Bertrand Chapron, and VN Kudryavtsev. Directional short wind wave spectra derived from the sea surface photography. *Journal of Geophysical Research: Oceans*, 118(9):4380–4394, 2013.

A

Appendix

List of Constants

The list describes all the constants that are used within the body of the document

α	Volumetric thermal expansion coefficient of water at $20°C$	$207 \times 10^{-6} K^{-1}$
α_g	Tuning parameter inside the gravity range	5×10^{-3}
γ	Surface tension of water at $20°C$	$0.07275 \mathrm{J/m^2}$
γ_d	Constant for computing divergence of the surface current	0.2
κ	Von Karman constant	0.4
$\overline{\theta_{\mathrm{wb}}}$	Mean tilt of the non-Bragg scattering area	$5 \cdot 10^{-2}$
ρ_a	Density of air at $15°C$	$1.225 \mathrm{kg/m^3}$
ρ_w	Density of water	$1000 \mathrm{kg/m^3}$
$\varepsilon_{\mathrm{wb}}$	Ratio of vertical to horizontal scale of the breaking zone	5×10^{-3}
ε_r	Relative dielectric constant of $25°C$ pure water at a frequency of 5.35 GHz	$73 + 18i$
a_*	Coefficient for computing the roughness scale	0.018
a_0	Constant for computing Elfouhaily's spreading function	$\ln(2)/4$
a_p	Constant for computing Elfouhaily's spreading function	4
a_v	Coefficient for computing the roughness scale	0.1
B_{wb}	Saturation spectrum for computing cross-polarization wave breaking NRCS	10^{-2}
b_r	Coefficient for the breaker wave number upper limit	0.1
c_b	Empirical constant for computing I_{sw}	4.5×10^{-3}
c_m	Minimum phase velocity at the gravity-capillary peak	$0.23 \mathrm{m/s}$
c_q	Coefficient for computing the fraction of wave breaking covered area	10.5
d	Division coefficient in composite model	$1/4$
f	Coriolis parameter in f-plane approximation	$10^{-4} s^{-1}$
g	Gravitational acceleration	$9.80665 m/s^2$
k_{wb}	Wave breaking wave number	$2\pi/0.3 rad/m$
n_γ	Tuning parameter inside the capillary-gravity range	1
n_g	Tuning parameter inside the gravity range	5
s^2_{wb}	Mean square slope of enhanced roughness (assumed isotropic) of the wave breaking zone	0.19
v	Kinematic viscosity coefficient of sea water at $20°C$	$1.15 \times 10^{-6} m^2/s$
v_a	Kinematic viscosity coefficient of air at $15°C$	$1.47 \times 10^{-5} m^2/s$
X_0	Dimensionless fetch	2.2×10^4